
Density-Informed Pseudo-Counts for Calibrated Evidential Deep Learning

Pietro Carlotti*

Department of Statistics and Data Sciences
University of Texas at Austin
pietro.carlotti@utexas.edu

Nevena Gligić*

Department of Statistics and Data Sciences
University of Texas at Austin
nevena.gligic@utexas.edu

Arya Farahi

Department of Statistics and Data Sciences
University of Texas at Austin
arya.farahi@austin.utexas.edu

Abstract

Evidential Deep Learning (EDL) is a popular framework for uncertainty-aware classification that models predictive uncertainty via Dirichlet distributions parameterized by neural networks. Despite its popularity, its theoretical foundations and behavior under distributional shift remain poorly understood. In this work, we provide a principled statistical interpretation by proving that EDL training corresponds to amortized variational inference in a hierarchical Bayesian model with a tempered pseudo-likelihood. This perspective reveals a major drawback: standard EDL conflates epistemic and aleatoric uncertainty, leading to systematic overconfidence on out-of-distribution inputs. To address this, we introduce Density-Informed Pseudo-count EDL, a new parametrization that decouples class prediction from uncertainty quantification by separately estimating the conditional label distribution and the marginal covariate density. This separation preserves evidence in high-density regions while shrinking predictions toward a uniform prior for out-of-distribution data. Theoretically, we prove that our method achieves asymptotic concentration. Empirically, we show our method enhances interpretability and improves robustness and uncertainty calibration under distributional shift.

1 Introduction

Uncertainty quantification is a central challenge in modern machine learning, particularly in safety-critical and high-stakes applications such as medical diagnosis [Begoli et al., 2019] and scientific discovery [Gal et al., 2022]. While deep neural networks achieve remarkable predictive accuracy, they are notoriously prone to overconfidence [Guo et al., 2017], especially under limited data or distributional shift [Seligmann et al., 2023, Mucsányi et al., 2024]. Reliable uncertainty estimates are therefore essential for calibrated decision-making, detection of out-of-distribution (OOD) inputs, robust deployment, and supporting downstream reasoning. Despite its importance, principled, scalable uncertainty quantification for deep models remains an open problem.

A wide range of methods has been proposed to address this challenge [Mucsányi et al., 2024, He et al., 2025]. Bayesian neural networks aim to capture epistemic uncertainty by placing priors over model parameters and performing posterior inference, typically via variational approximations or Monte Carlo sampling [Blundell et al., 2015, Hernández-Lobato and Adams, 2015, Gal and Ghahramani,

*Equal contribution.

2016]. Ensemble-based methods approximate posterior uncertainty by aggregating predictions from multiple trained models, yielding strong empirical performance at the cost of increased computational burden [Lakshminarayanan et al., 2017, Wang and Ji, 2023]. Alternatively, post-hoc calibration methods adjust predictive confidence without explicitly modeling uncertainty [Guo et al., 2017, Gibbs et al., 2025, Vashistha and Farahi, 2025]. While effective in certain problems, these approaches often suffer from scalability, complex training pipelines, or limited interpretability of uncertainty estimates.

Evidential Deep Learning (EDL) offers an alternative that directly models predictive uncertainty at the output level [Sensoy et al., 2018]. Rather than placing distributions over network parameters, EDL predicts a distribution over class probabilities by parameterizing a Dirichlet distribution with a neural network. This formulation provides a unified representation of predictive confidence and uncertainty, allows for single forward-pass inference, and integrates naturally with standard deep learning pipelines. Hence, EDL has gained popularity as a practical framework for uncertainty-aware classification [Gao et al., 2025]. The main idea of EDL is to map the covariates $X \in \mathbb{R}^d$ to a distribution over the class probabilities $p \in \Delta^{K-1}$ for a categorical response variable $Y \in \{1, \dots, K\}$. The original formulation of Sensoy et al. [2018] achieve this by specifying the distribution of the class probabilities using a Dirichlet distribution with concentration parameters given by a neural network $\text{NN}^\phi : \mathbb{R}^d \rightarrow \mathbb{R}_+^K$ with parameters ϕ which outputs a K -dimensional vector of non-negative weights.

To train this model, Sensoy et al. [2018] propose a class of loss functions with a structure

$$\mathcal{L}_{\text{EDL}}^\lambda(\phi) = \mathcal{L}_{\text{data}}(\phi) + \lambda \mathcal{L}_{\text{reg}}(\phi), \quad (1)$$

where $\mathcal{L}_{\text{data}}$ encourages the model to fit the training data, \mathcal{L}_{reg} penalizes complexity, and $\lambda > 0$ is a hyperparameter that balances the trade-off between the two. In particular, we will focus on the specific choice of data and regularization terms proposed by Sensoy et al. [2018]:

$$\begin{aligned} \mathcal{L}_{\text{data}}(\phi) &= \sum_{i=1}^n -\mathbb{E}_{\text{Dir}(\alpha + \text{NN}_{X_i}^\phi)} [\log \text{Cat}(Y_i | p_i)], \\ \mathcal{L}_{\text{reg}}(\phi) &= \sum_{i=1}^n \text{KL} \left(\text{Dir}(\alpha + \text{NN}_{X_i}^\phi) \parallel \text{Dir}(\alpha) \right), \end{aligned} \quad (2)$$

where $\alpha \in \mathbb{R}_+^K$ is prior concentration parameters. Despite its intuitive appeal and empirical success, the theoretical foundations of EDL and its behavior under distributional shift remain poorly understood. In particular, it is unclear how the learned Dirichlet distributions relate to the underlying data-generating process (DGP), and whether EDL can meaningfully distinguish among different sources of uncertainty. See Appendix B for a more detailed review of related work on EDL and its limitations.

In this work, we provide a statistical interpretation of the EDL framework, elucidate the role of the regularization parameter, and propose a novel parametrization, Density-Informed Pseudo-count EDL (DIP-EDL), with the goal of improving performance for both in-distribution and out-of-distribution settings. DIP-EDL is a principled method that decouples class prediction from uncertainty quantification by separately estimating the conditional label distribution and the marginal covariate density.

2 Statistical Interpretation of EDL

Here, we present a unifying interpretation of EDL: (i) a hierarchical Bayesian model with amortized variational inference (VI), and (ii) an empirical risk minimization (ERM) approach. We show that both formulations yield the same optimization objective, thereby providing a statistical interpretation and clarifying the uncertainty quantification properties of EDL methods.

2.1 Problem Setup

Suppose the observed data is generated according to the DGP

$$(Y_i, X_i) \stackrel{\text{i.i.d.}}{\sim} P_{Y,X}^*, \quad i = 1, \dots, n. \quad (3)$$

The joint distribution admits the factorization $P_{Y,X}^* = P_{Y|X}^* P_X^*$, where $P_{Y|X}^*$ denotes the conditional distribution of Y given X , and P_X^* the marginal distribution of X . Throughout the analysis, we assume that P_X^* is absolutely continuous with respect to the Lebesgue measure on \mathbb{R}^d . Our goal is to estimate $P_{Y|X}^*$ and provide calibrated uncertainty quantification for in- and out-of-sample predictions.

2.2 Amortized VI

We show that EDL admits an interpretation as amortized VI on a modification of the Independent Categorical-Dirichlet (ICD) model, in which class probabilities vary across observations.

Definition 2.1. ICD Model. For some $\alpha \in \mathbb{R}_+^K$, the model is defined as follows:

$$\begin{aligned} Y_i | p_i &\stackrel{\text{i.i.d.}}{\sim} f_{p_i} = \text{Cat}(p_i), \quad i = 1, \dots, n, \\ p_i &\stackrel{\text{i.i.d.}}{\sim} \pi = \text{Dir}(\alpha), \quad i = 1, \dots, n. \end{aligned}$$

This prior is convenient because its conjugacy with the categorical likelihood allows the posterior of class probabilities to be computed in closed form, as summarized in the following proposition.

Proposition 2.2. *Given Definition 2.1, the posterior and posterior predictive distributions are*

$$\pi_{Y_i} = \text{Dir}(\alpha + e_{Y_i}), \quad i = 1, \dots, n, \quad p_{1:n} | Y_{1:n} \sim \prod_{i=1}^n \pi_{Y_i}, \quad Y_{n+1} | Y_{1:n} \sim \text{Cat}\left(\frac{\alpha}{\alpha_0}\right),$$

where $e_{Y_i} \in \{0, 1\}^K$ denotes the one-hot encoding of Y_i , $i = 1, \dots, n$, and $\alpha_0 = \sum_{k=1}^K \alpha_k$.

Despite its analytical tractability, this model neglects covariates entirely. While a covariate-indexed extension can incorporate them (see Appendix C.2), its applicability is limited to discrete inputs. Because P_X^* is continuous, each observation is almost surely unique, preventing information sharing. To address this, we introduce covariate dependence via amortized VI [Margossian and Blei, 2023].

Definition 2.3. Amortized VI for the ICD Model. Given Definition 2.1, we approximate the posterior via a mean-field variational family:

$$p_{1:n} | Y_{1:n} \approx q_{X_{1:n}}^{\hat{\phi}_n} = \underset{q_{X_{1:n}}^{\phi}}{\text{argmin}} \left\{ \text{KL} \left(q_{X_{1:n}}^{\phi} \parallel \pi_{Y_{1:n}} \right) \right\},$$

where

$$q_{X_{1:n}}^{\phi} = \prod_{i=1}^n q_{X_i}^{\phi} \quad \text{and} \quad q_{X_i}^{\phi} = \text{Dir} \left(\alpha + \text{NN}^{\phi}(X_i) \right), \quad i = 1, \dots, n,$$

$\text{NN}^{\phi} : \mathbb{R}^d \rightarrow \mathbb{R}_+^K$ is a neural network with $\phi \in \Phi$, Φ is the neural network class, with parameters

$$\hat{\phi}_n = \underset{\phi \in \Phi}{\text{argmin}} \left\{ \text{KL} \left(q_{X_{1:n}}^{\phi} \parallel \pi_{Y_{1:n}} \right) \right\}. \quad (4)$$

Parameterizing the variational family via a neural network is convenient because it enables non-trivial predictions at arbitrary new covariate values X_{n+1} , as formalized in the following proposition.

Proposition 2.4. *Given Definitions 2.1 and 2.3, the posterior predictive distribution is*

$$Y_{n+1} | Y_{1:n}, X_{1:n+1} \approx \text{Cat} \left(\frac{\alpha + \text{NN}_{X_{n+1}}^{\hat{\phi}_n}}{\alpha_0 + S_{X_{n+1}}^{\hat{\phi}_n}} \right), \quad \text{where} \quad S_{X_{n+1}}^{\hat{\phi}_n} = \sum_{k=1}^K \text{NN}_{X_{n+1}}^{\hat{\phi}_n}(k).$$

In particular, carrying out the VI in Definition 2.3 reduces to the following minimization problem.

Proposition 2.5. *The optimization problem from Equation (4) is equivalent to minimizing*

$$\sum_{i=1}^n -\mathbb{E}_{q_{X_i}^{\phi}} [\log f_{p_i}(Y_i)] + \text{KL}(q_{X_i}^{\phi} \parallel \pi). \quad (5)$$

The objective in Proposition 2.5 matches the EDL loss in Equation (1) but lacks a regularization hyperparameter; we resolve this by introducing a temperature parameter into a new model.

Definition 2.6. Tempered ICD Model. The model is defined as follows:

$$\begin{aligned} Y_i | p_i &\stackrel{\text{i.i.d.}}{\propto} f_{p_i}^{\nu} = \prod_{k=1}^K p_i(k)^{\nu \mathbb{I}(Y_i=k)}, \quad i = 1, \dots, n, \\ p_i &\stackrel{\text{i.i.d.}}{\sim} \pi = \text{Dir}(\alpha), \quad i = 1, \dots, n, \end{aligned}$$

for some $\alpha \in \mathbb{R}_+^K$ and $\nu > 0$.

This modified model is motivated by using a tempered likelihood [Bissiri et al., 2016], which provides explicit control over the data’s influence on the posterior via the parameter ν , thereby introducing an additional degree of freedom in the trade-off between data fit and regularization.

Notice that for $\nu \neq 1$, the categorical likelihood $f_{p_i}^\nu$ is unnormalized. A valid likelihood would require a normalizing constant dependent on both p_i and ν . Instead of renormalizing, we follow a standard strategy in generalized Bayesian methods by treating the unnormalized likelihood as a pseudo-likelihood for posterior updating [Ventura and Racugno, 2016].

Under the tempered ICD model, the posterior and posterior predictive distributions remain tractable.

Proposition 2.7. *Given Definition 2.6, the posterior and posterior predictive distributions are*

$$\pi_{Y_i}^\nu = \text{Dir}(\alpha + \nu e_{Y_i}), \quad i = 1, \dots, n, \quad p_{1:n} | Y_{1:n} \sim \pi_{Y_{1:n}}^\nu = \prod_{i=1}^n \pi_{Y_i}^\nu, \quad Y_{n+1} | Y_{1:n} \sim \text{Cat}\left(\frac{\alpha}{\alpha_0}\right).$$

Once again, we approximate this posterior via amortized VI to enable predictions at new inputs.

Definition 2.8. Amortized VI for the Tempered ICD Model. Given Definition 2.6, we approximate the posterior via a mean-field variational family:

$$p_{1:n} | Y_{1:n} \approx q_{X_{1:n}}^{\hat{\phi}_n} = \underset{q_{X_{1:n}}^\phi}{\text{argmin}} \left\{ \text{KL}\left(q_{X_{1:n}}^\phi \parallel \pi_{Y_{1:n}}^\nu\right) \right\},$$

where $q_{X_{1:n}}^\phi$, NN^ϕ , and Φ are defined as in Definition 2.3, and

$$\hat{\phi}_n = \underset{\phi \in \Phi}{\text{argmin}} \left\{ \text{KL}\left(q_{X_{1:n}}^\phi \parallel \pi_{Y_{1:n}}^\nu\right) \right\}$$

are the learned parameters.

We are now ready to state the main theoretical result of this paper. Applying amortized VI to the Tempered ICD Model is exactly equivalent to EDL training under the loss in Equation (1).

Theorem 2.9. *Given Definitions 2.6 and 2.8, the amortized VI objective is equivalent to EDL training:*

$$\hat{\phi}_n = \underset{\phi \in \Phi}{\text{argmin}} \left\{ \mathcal{L}_{\text{EDL}}^{\frac{1}{\nu}}(\phi; Y_{1:n}, X_{1:n}) \right\}. \quad (6)$$

This statistical interpretation clarifies EDL’s uncertainty mechanism: because the objective is a KL divergence, we can characterize the conditions satisfied by the learned parameters at convergence.

Proposition 2.10. *Given Definitions 2.6 and 2.8, if Φ is sufficiently expressive and the optimization procedure attains the global minimum of the objective, then $\hat{\phi}_n$ satisfies*

$$\text{NN}_{X_i}^{\hat{\phi}_n} = \nu e_{Y_i}, \quad i = 1, \dots, n. \quad (7)$$

This result has a direct implication for uncertainty quantification. In particular, consider the following uncertainty measure introduced by Sensoy et al. [2018].

Definition 2.11. Vacuity. Let $\alpha_X \in \mathbb{R}_+^K$ be the concentration parameters of a Dirichlet distribution possibly depending on covariates $X \in \mathbb{R}^d$. Then, its vacuity is defined as

$$u(\alpha_X) = \frac{K}{a_0^X} \quad \text{where} \quad a_0^X = \sum_{k=1}^K \alpha_X(k). \quad (8)$$

In this setting, perfect interpolation implies that the uncertainty associated with in-sample probability vectors is constant across all training points and is fully determined by the temperature parameter ν .

Proposition 2.12. *Given Definitions 2.6 and 2.8, if the condition in Equation (7) is satisfied, then*

$$u\left(\alpha + \text{NN}_{X_i}^{\hat{\phi}_n}\right) = \frac{K}{\alpha_0 + \nu}, \quad i = 1, \dots, n. \quad (9)$$

This demonstrates that EDL depends fundamentally on the temperature parameter ν , rendering its uncertainty quantification spurious without meaningful tuning. These results corroborate recent theoretical critiques of EDL. Specifically, Bengs et al. [2022] and Shen et al. [2024] demonstrate that the reliance on a hyper-parameter to balance likelihood evidence against prior regularization introduces a fundamental arbitrariness into the uncertainty quantification process which can be theoretically problematic. For example, aleatoric uncertainty should represent a fixed constant of irreducible noise inherent to the data, yet in EDL, it changes depending on a user-defined hyperparameter.

2.3 ERM

An alternative interpretation of the EDL framework arises from the ERM perspective.

Definition 2.13. EDL as ERM. Given the DGP given in Equation (3), consider the loss function

$$l^\nu(\phi; y, x) = \text{KL}(q_x^\phi \parallel \pi_y^\nu),$$

where q_x^ϕ is the variational distribution from Definition 2.8 and π_y^ν is the posterior from Definition 2.6. The parameter ϕ is learned by minimizing the empirical risk, with corresponding expected risk:

$$\widehat{\mathcal{R}}_n^\nu(\phi) = \frac{1}{n} \sum_{i=1}^n l^\nu(\phi; Y_i, X_i), \quad \mathcal{R}^\nu(\phi) = \mathbb{E}_{P_{Y,X}^*} [l^\nu(\phi; Y, X)].$$

This formulation clarifies the EDL objective as an empirical estimator of an expected value.

Theorem 2.14. *Given Definition 2.13, the empirical risk and the EDL loss are proportional:*

$$\widehat{\mathcal{R}}_n^\nu(\phi) = \frac{\nu}{n} \mathcal{L}_{\text{EDL}}^{\frac{1}{\nu}}(\phi; Y_{1:n}, X_{1:n}).$$

This theorem clarifies the specific quantities targeted by the EDL training objective.

Theorem 2.15. *Given Definition 2.13, if Φ is sufficiently expressive, it follows that*

$$q_X^{\phi^*} = \text{Dir}(\alpha + \nu P_{Y|X}^*) \quad \text{where} \quad \phi^* = \underset{\phi \in \Phi}{\text{argmin}} \{ \mathcal{R}^\nu(\phi) \}.$$

Thus, even with the oracle $P_{Y|X}^*$, the uncertainty quantification remains governed by ν .

Proposition 2.16. *Given Definition 2.13, if the condition in Theorem 2.15 holds, then*

$$u(\alpha + \nu P_{Y|X}^*) = \frac{K}{\alpha_0 + \nu}.$$

Thus, the temperature parameter dictates uncertainty regardless of data fit, and vacuity persists even as sample size grows. Our results align with Shen et al. [2024], who also note that EDL does not distinguish epistemic from aleatoric uncertainty because vacuity remains constant regardless of the amount of data. Appendix G provides an empirical validation of this result in a controlled toy setting.

3 Choice of the Temperature Parameter

The temperature parameter ν determines the uncertainty produced by EDL. Theorem 2.15 shows that EDL does not jointly learn the conditional label distribution and the associated uncertainty. It learns only the conditional distribution, while uncertainty is imposed externally through ν . Consequently, although EDL is framed as optimizing both prediction and uncertainty quantification, it only resolves the predictive task, leaving uncertainty calibration fundamentally dependent on the choice of temperature. Given this insight, we avoid manual specification of ν or hyperparameter tuning on arbitrary predictive metrics. Instead, we seek a principled choice based on two desiderata:

1. **Distributional awareness:** Uncertainty is higher in low-density regions of the covariate space, reflecting limited information about the conditional label distribution.
2. **Asymptotic consistency:** Epistemic uncertainty vanishes as the number of samples grows, whereas aleatoric uncertainty may persist due to inherent noise in the data.

The intuition for these criteria stems from Theorem 2.15, which suggests interpreting $\nu P_{Y|X}^*$ as a label count vector where ν acts as a pseudo-count. However, as a global parameter, ν fails to account for the sample size or the covariate distribution. To address this, we introduce a notion of covariate proximity so that similar observations can share information. This ensures that labels from nearby training points have lower uncertainty, while regions lacking nearby data reflect increased uncertainty.

Building on this local perspective, we consider a small neighborhood around a covariate value x within a sample of size n . In a sufficiently small region, the expected number of observations is approximately $n P_X^*(x)$, and the expected number of labels belonging to class k is $n P_X^*(x) P_{Y|X}^*(k | x)$. This relationship provides a principled foundation for choosing ν .

Definition 3.1. DIP-EDL. Given Definition 2.8, we replace the variational family with

$$q_{X_i}^{\psi, \phi} = \text{Dir} \left(\alpha + n \text{DE}_{X_i}^{\psi} \text{NN}_{X_i}^{\phi} \right), \quad i = 1, \dots, n, \quad (10)$$

where $\text{DE}^{\psi} : \mathbb{R}^d \rightarrow \mathbb{R}_+$ is a density estimator for P_X^* with $\psi \in \Psi$, and $\text{NN}^{\phi} : \mathbb{R}^d \rightarrow \mathbb{R}_+^K$ is a neural network estimator for $P_{Y|X}^*$ with $\phi \in \Phi$.

From an applied perspective, this specification is convenient for several reasons. First, it enables independent training of the density estimator and the neural network, making practical implementation straightforward. Second, it is architecture-agnostic: any density estimator and classifier can be used, and they may be trained with any loss functions suitable for density estimation and classification, provided they correctly learn the target distributions at least asymptotically. Crucially, while our exposition focuses on neural networks, DIP-EDL does not require the classifier to be differentiable. Unlike other EDL methods, which train a neural network end-to-end through the EDL loss and thus require gradient-based optimization, DIP-EDL accommodates any off-the-shelf classifier, including non-differentiable models (e.g., random forests), enabling principled uncertainty quantification for arbitrary classifier classes. Third, like other EDL-based approaches, DIP-EDL requires only a single forward pass at inference time, avoiding the computational overhead of methods that rely on multiple forward passes (e.g., deep ensembles and MC Dropout).

Beyond these practical properties, DIP-EDL also satisfies both proposed theoretical criteria. Regarding distributional awareness, the posterior predictive distribution contracts toward the prior in low-density regions where nearby training samples are scarce. Furthermore, the model achieves asymptotic consistency because q_{X_i} concentrates around the true conditional distribution $P_{Y|X}^*(\cdot | X_i)$.

Theorem 3.2. *Given the DGP (3) and Definition 3.1, consistent estimation of P_X^* and $P_{Y|X}^*$ implies pointwise asymptotic concentration in probability of the approximate posterior:*

$$\text{DE}_{X_i}^{\hat{\psi}_n} \xrightarrow{P} P_X^*(X_i), \quad \text{NN}_{X_i}^{\hat{\phi}_n} \xrightarrow{P} P_{Y|X}^*(\cdot | X_i) \quad \Rightarrow \quad p_i | X_{1:n}, Y_{1:n} \approx q_{X_i}^{\hat{\psi}_n, \hat{\phi}_n} \xrightarrow{P} P_{Y|X}^*(\cdot | X_i).$$

Prior work has shown that incorporating the inputs or latent representation density improves uncertainty estimates [e.g., Mukhoti et al., 2021, Bui and Liu, 2024, Yoon and Kim, 2024, Van Katwyk and Bergen, 2025]. But, unlike these approaches, which treat covariate density as an ad-hoc component to enforce epistemic uncertainty, our method’s dependence on it emerges naturally from the model formulation. This yields a more principled representation and superior empirical performance.

DIP-EDL conceptually resembles Posterior Network [PostNet, Charpentier et al., 2020], as both rely on density-based pseudo-counts to specify the approximate posterior over class probabilities. However, the two methods differ in key aspects. First, PostNet uses a different factorization of the pseudo-counts. DIP-EDL decomposes the pseudo-count of observations with label k in a neighborhood of x as $n P_X^*(x) P_{Y|X}^*(k | x)$, while PostNet uses the opposite factorization $n P_Y^*(k) P_{X|Y}^*(x | k)$, where P_Y^* is the marginal class distribution and $P_{X|Y}^*$ is the class-conditional density in the input space. More importantly, PostNet estimates $P_{X|Y}^*$ via $P_{Z|Y}^*$, where Z is a learned latent representation of the input, which empirically leads to degraded performance compared to our decomposition.

With that being said, despite this connection, our approach offers three primary advantages:

- **Direct Calibration:** It ties uncertainty directly to observable predictive outputs, resulting in improved empirical performance (see Section 4.2).
- **Modularity:** Unlike PostNet, which relies on a single training objective to learn the covariate density and conditional label distribution, DIP-EDL estimates these components separately. This separation allows for a more flexible and modular training process.
- **Efficiency:** DIP-EDL has the potential to be much more computationally efficient as it requires only a single density estimator for the entire input space rather than one per class, which can be practically challenging when the number of classes is large.

4 Experiments

4.1 Experimental Configuration

Datasets. We use MNIST Deng [2012] and CIFAR-10 Krizhevsky et al. [2009] as ID datasets. For OOD evaluation, we use K-MNIST Clanuwat et al. [2018] and Omniglot Lake et al. [2015]

for MNIST, and **CIFAR-100** Krizhevsky [2009] and **SVHN** Netzer et al. [2011] for CIFAR-10, covering both near-OOD (digits vs. characters) and far-OOD (digits vs. natural images) scenarios. Additionally, we perform experiments on a real scientific dataset **LAMOST Data Release 9 (DR9)** Cui et al. [2012]. We treat Galaxy and Quasar classes as ID, while we leave the class star as OOD.

Baselines. We benchmark against four Dirichlet-based baselines: **EDL** Sensoy et al. [2018], **R-EDL** Chen et al. [2024a], **Re-EDL** Chen et al. [2025], **DAEDL** Yoon and Kim [2024], and **PostNet** Charpentier et al. [2020], which require no OOD training data and operate in a single forward pass, similarly to our method. We additionally compare DIP-EDL against **MC-Dropout** Gal and Ghahramani [2016] and **Deep Ensembles** Lakshminarayanan et al. [2017], which require multiple forward passes at inference time.

Implementation Details. We tailor model architectures to each dataset. For MNIST, we use **LeNet-5** Lecun et al. [1998] following Sensoy et al. [2018], with a Masked Autoregressive Flow (**MAF**) Papamakarios et al. [2017] on the flattened pixel space for density estimation. For CIFAR-10, we use **WideResNet-28-10** Zagoruyko and Komodakis [2016] with Gaussian Discriminant Analysis (**GDA**) Hastie and Tibshirani [1996] fitted on the resulting 640-dimensional embeddings. For LAMOST, we use a **multi-branch 1D CNN** (Shi) designed for stellar spectra classification, with **GDA** fitted on 32-dimensional penultimate features. See Appendix D for details.

Performance Metrics. Following the OOD detection literature Chen et al. [2024a], Yoon and Kim [2024], Charpentier et al. [2020], we report three metrics: **classification accuracy** on the ID test set; **AUROC** (Area Under the Receiver Operating Characteristic curve) and **AUPR** (Area Under the Precision-Recall curve), which rank OOD samples (positive class) higher in uncertainty than ID samples (negative class). The Brier Score (**BS**) additionally measures predicted probability magnitudes against one-hot targets for ID data and a uniform distribution for OOD data, penalizing high-confidence predictions on unseen domains even when correctly ranked as uncertain.

4.2 Experiments with MNIST as ID dataset

On MNIST, Table 1, **DIP-EDL** achieves the highest classification accuracy (99.53%) and lowest ID Brier Score (0.01) across all methods, including MC-Dropout and Deep Ensembles, improving calibration over EDL (0.19) and DAEDL (0.02).

These improvements extend to OOD detection. DIP-EDL achieves AUROC of 0.99 on both OOD datasets, outperforming all baselines. On Omniglot, AUROC is near-saturated across methods, but DIP-EDL yields the lowest OOD BS, unlike PostNet, MC-Dropout, and Deep Ensembles, which exhibit high OOD BS despite strong AUROC, indicating overconfidence under distributional shift.

Table 1: **MNIST: ID and OOD performance.** ID accuracy and calibration, with OOD detection against K-MNIST (near-OOD) and Omniglot (far-OOD). Results are $\mu \pm \sigma$ over 4 runs.

| Model | ID Performance | | OOD Performance Metrics | | | | | |
|----------------------|---------------------------------------|---------------------------------------|---------------------------------------|---------------------------------------|---------------------------------------|---------------------------------------|---------------------------------------|---------------------------------------|
| | Acc. (\uparrow) | BS (\downarrow) | AUROC (\uparrow) | | AUPR (\uparrow) | | OOD BS (\downarrow) | |
| | | | K-MNIST | Omniglot | K-MNIST | Omniglot | K-MNIST | Omniglot |
| EDL | 0.9166 \pm 0.0498 | 0.1886 \pm 0.0434 | 0.9116 \pm 0.0340 | 0.9204 \pm 0.0477 | 0.8622 \pm 0.0588 | 0.8566 \pm 0.0778 | 0.0569 \pm 0.0080 | 0.0185 \pm 0.0032 |
| R-EDL | 0.9940 \pm 0.0005 | 0.0113 \pm 0.0009 | 0.9729 \pm 0.0014 | 0.9879 \pm 0.0026 | 0.9599 \pm 0.0025 | 0.9818 \pm 0.0055 | 0.1755 \pm 0.0192 | 0.0726 \pm 0.0372 |
| Re-EDL | 0.9940 \pm 0.0010 | 0.0100 \pm 0.0010 | 0.9910 \pm 0.0010 | 1.0000 \pm 0.0000 | 0.9890 \pm 0.0020 | 1.0000 \pm 0.0000 | 0.7050 \pm 0.0160 | 0.5430 \pm 0.0310 |
| DAEDL | 0.9937 \pm 0.0005 | 0.0225 \pm 0.0014 | 0.9987 \pm 0.0003 | 0.9997 \pm 0.0002 | 0.9981 \pm 0.0006 | 0.9995 \pm 0.0002 | 0.0097 \pm 0.0018 | 0.0000 \pm 0.0000 |
| PostNet | 0.9925 \pm 0.0009 | 0.0117 \pm 0.0017 | 0.9602 \pm 0.0128 | 0.9936 \pm 0.0026 | 0.9570 \pm 0.0111 | 0.9862 \pm 0.0053 | 0.4922 \pm 0.0184 | 0.2816 \pm 0.0514 |
| MC Dropout | 0.9940 \pm 0.0000 | 0.0090 \pm 0.0010 | 0.9800 \pm 0.0020 | 0.9880 \pm 0.0010 | 0.9760 \pm 0.0020 | 0.9820 \pm 0.0030 | 0.6150 \pm 0.0060 | 0.4800 \pm 0.0390 |
| Deep Ensemble | 0.9940 \pm 0.0000 | 0.0100 \pm 0.0010 | 0.9830 \pm 0.0010 | 0.9970 \pm 0.0010 | 0.9810 \pm 0.0010 | 0.9980 \pm 0.0010 | 0.6090 \pm 0.0060 | 0.3840 \pm 0.0460 |
| DIP-EDL | 0.9953 \pm 0.0003 | 0.0081 \pm 0.0005 | 0.9997 \pm 0.0000 | 0.9998 \pm 0.0000 | 0.9995 \pm 0.0001 | 0.9996 \pm 0.0001 | 0.0013 \pm 0.0002 | 0.0000 \pm 0.0000 |

4.3 Experiments with CIFAR-10 as ID dataset

On CIFAR-10 (Table 2) a more challenging setting compared to MNIST, DIP-EDL achieves the highest accuracy (95.03%) and lowest ID BS (0.0978) among single-pass methods. Deep Ensembles, using multiple forward passes, achieves better ID performance at the cost of inference efficiency.

For OOD detection, performance trends differ between near- and far-shift scenarios. On the far-OOD task (SVHN), DIP-EDL achieves the highest AUROC (0.9660) and AUPR (0.9830), outperforming all baselines including Deep Ensembles (0.9628 AUROC, 0.9802 AUPR). On the near-OOD task (CIFAR-100), which shares significant visual overlap with CIFAR-10 and is thus more challenging, scores are more closely matched with Deep Ensembles, which achieves the highest AUROC (0.9072), while DIP-EDL achieves the second highest AUROC (0.9002) and the highest AUPR (0.8859). These results confirm reliable distributional shift detection by DIP-EDL, particularly for far-OOD scenarios.

DIP-EDL also achieves the second-lowest OOD BS across both OOD datasets, surpassing Deep Ensembles. This reflects well-calibrated epistemic uncertainty, arising from accurate feature representation in lower-dimensional feature space, together with precise density estimation on it, which keeps likelihoods sufficiently small to offset classifier confidence. EDL achieves the lowest OOD BS but at the cost of poor AUROC and AUPR, indicating uninformative uniform predictions rather than meaningful uncertainty. DIP-EDL is the only method that simultaneously achieves strong ranking (AUROC/AUPR) *and* strong calibration (OOD BS) on out-of-distribution data. The impact of individual components is corroborated by the ablation study (Section 4.5), and the effect of corrupted likelihood estimates on the overall DIP-EDL performance is discussed in Appendix H. Difficulty of density estimation in MNIST versus CIFAR-10 experiments is visualized in Appendix E.

Table 2: **CIFAR-10: ID and OOD performance.** ID accuracy and calibration, with OOD detection against CIFAR-100 (near-OOD) and SVHN (far-OOD). Results are $\mu \pm \sigma$ over 4 runs.

| Model | ID Performance | | OOD Performance Metrics | | | | | |
|----------------------|---------------------------------------|---------------------------------------|---------------------------------------|---------------------------------------|---------------------------------------|---------------------------------------|---------------------------------------|---------------------------------------|
| | Acc. (\uparrow) | BS (\downarrow) | AUROC (\uparrow) | | AUPR (\uparrow) | | OOD BS (\downarrow) | |
| | | | CIFAR-100 | SVHN | CIFAR-100 | SVHN | CIFAR-100 | SVHN |
| EDL | 0.7535 \pm 0.1526 | 0.3520 \pm 0.1355 | 0.7588 \pm 0.0880 | 0.7519 \pm 0.1465 | 0.6900 \pm 0.0956 | 0.8094 \pm 0.0992 | 0.0960 \pm 0.0326 | 0.0492 \pm 0.0067 |
| R-EDL | 0.8957 \pm 0.0030 | 0.1737 \pm 0.0040 | 0.8484 \pm 0.0040 | 0.8741 \pm 0.0101 | 0.8016 \pm 0.0051 | 0.9150 \pm 0.0096 | 0.3603 \pm 0.0123 | 0.3262 \pm 0.0396 |
| Re-EDL | 0.8939 \pm 0.0009 | 0.1737 \pm 0.0020 | 0.8603 \pm 0.0020 | 0.9102 \pm 0.0059 | 0.8229 \pm 0.0039 | 0.9427 \pm 0.0058 | 0.6613 \pm 0.0108 | 0.6303 \pm 0.0173 |
| DAEDL | 0.8879 \pm 0.0024 | 0.1760 \pm 0.0026 | 0.8323 \pm 0.0015 | 0.8606 \pm 0.0135 | 0.7913 \pm 0.0015 | 0.9088 \pm 0.0153 | 0.4087 \pm 0.0079 | 0.3843 \pm 0.0426 |
| PostNet | 0.8169 \pm 0.0127 | 0.2623 \pm 0.0159 | 0.7691 \pm 0.0113 | 0.7760 \pm 0.0342 | 0.7254 \pm 0.0139 | 0.8532 \pm 0.0229 | 0.4609 \pm 0.0271 | 0.4734 \pm 0.0687 |
| MC Dropout | <i>0.9534 \pm 0.0011</i> | <i>0.0729 \pm 0.0008</i> | 0.8833 \pm 0.0032 | 0.8802 \pm 0.0223 | 0.8407 \pm 0.0034 | 0.9053 \pm 0.0153 | 0.5958 \pm 0.0059 | 0.6111 \pm 0.0513 |
| Deep Ensemble | 0.9614 \pm 0.0006 | 0.0587 \pm 0.0007 | 0.9072 \pm 0.0009 | <i>0.9628 \pm 0.0056</i> | <i>0.8807 \pm 0.0009</i> | <i>0.9802 \pm 0.0037</i> | 0.5222 \pm 0.0016 | 0.4200 \pm 0.0302 |
| DIP-EDL | 0.9503 \pm 0.0017 | 0.0978 \pm 0.0014 | <i>0.9002 \pm 0.0006</i> | 0.9660 \pm 0.0034 | 0.8859 \pm 0.0003 | 0.9830 \pm 0.0028 | <i>0.3251 \pm 0.0044</i> | <i>0.1109 \pm 0.0088</i> |

4.4 Experiments with LAMOST as ID dataset

On LAMOST stellar spectra dataset (Table 3; dimension 3000), the ID task is Galaxy/Quasar classification with Star spectra as OOD. LAMOST is the most challenging setting in this benchmark, with severe class imbalance causing several methods to degenerate. EDL exhibits near-random accuracy with high variance across seeds, while R-EDL and DAEDL plateau at the Quasar fraction in the training set, indicating majority-class collapse. Among the remaining methods, DIP-EDL ties Deep Ensembles for the highest accuracy (0.8929) and achieves the lowest ID Brier Score (0.1555) among single-model approaches, surpassed marginally by Deep Ensembles.

OOD scores are moderate across all methods, reflecting two inherent difficulties of this task: Star spectra share low-level spectral features with the ID classes, and the limited effective training set size constrains the quality of density estimates. Deep Ensembles achieves the highest AUROC, with DIP-EDL second (0.6789), both well above the remaining baselines. AUPR is uniformly high across methods due to the large proportion of Star spectra, making it an uninformative discriminator in this setting. PostNet achieves the lowest OOD BS but near-random AUROC, paralleling EDL on CIFAR-10. DIP-EDL is the strongest single-model method on this benchmark, achieving competitive ID classification and OOD detection performance on a real-world dataset where most baselines fail.

Table 3: **LAMOST: ID and OOD performance.** ID accuracy and calibration, with OOD detection against Star spectra. Results are $\mu \pm \sigma$ over 4 runs.

| Model | ID Performance | | OOD Performance Metrics | | |
|----------------------|---------------------------------------|---------------------------------------|---------------------------------------|---------------------------------------|---------------------------------------|
| | Acc. (\uparrow) | BS (\downarrow) | AUROC (\uparrow) | AUPR (\uparrow) | OOD BS (\downarrow) |
| | | | Star | Star | Star |
| EDL | 0.4955 \pm 0.2707 | 0.7585 \pm 0.4638 | 0.4934 \pm 0.1710 | 0.9884 \pm 0.0053 | 0.3595 \pm 0.2033 |
| R-EDL | 0.7706 \pm 0.0096 | 0.4273 \pm 0.0728 | 0.6022 \pm 0.1055 | 0.9933 \pm 0.0026 | 0.0783 \pm 0.0796 |
| Re-EDL | 0.7706 \pm 0.0096 | 0.4272 \pm 0.0728 | 0.5957 \pm 0.0990 | 0.9932 \pm 0.0024 | <i>0.0752 \pm 0.0764</i> |
| DAEDL | 0.7706 \pm 0.0096 | 0.2802 \pm 0.0028 | 0.5748 \pm 0.0138 | 0.9904 \pm 0.0004 | 0.1418 \pm 0.0054 |
| PostNet | 0.7328 \pm 0.0449 | 0.4231 \pm 0.0662 | 0.5315 \pm 0.1036 | 0.9913 \pm 0.0027 | 0.0297 \pm 0.0226 |
| MC Dropout | 0.5851 \pm 0.2215 | 0.6055 \pm 0.2897 | 0.4974 \pm 0.1334 | 0.9886 \pm 0.0051 | 0.3729 \pm 0.1132 |
| Deep Ensemble | 0.8929 \pm 0.0133 | 0.1497 \pm 0.0076 | 0.7425 \pm 0.0191 | 0.9957 \pm 0.0006 | 0.2394 \pm 0.0377 |
| DIP-EDL | 0.8929 \pm 0.0115 | <i>0.1555 \pm 0.0059</i> | <i>0.6789 \pm 0.0389</i> | <i>0.9948 \pm 0.0010</i> | 0.2517 \pm 0.0432 |

4.5 Ablation Study

We ablate DIP-EDL’s three components to isolate their contributions: (i) training set size, (ii) the density estimator, and (iii) the discriminative classifier. The results (Table 4) confirm the distinct role of each component: excluding the discriminative classifier yields near-random accuracy, while excluding the density estimator yields near-random OOD detection. Full results are in Appendix F.

Specifically, the training set size acts as a scaling factor required for concentration (Theorem 3.2), with no effect on ID accuracy or OOD ranking. Scaling by n increases Dirichlet concentration parameters proportionally, improving ID calibration (ID BS) while amplifying OOD deviation from the uniform prior (OOD BS), as seen in configurations 3–4 of Table 4. Without scaling by the sample size and the density estimator, ID calibration degrades even when ID accuracy is preserved (Appendix F). The effect of n on OOD BS is more pronounced on CIFAR-10 than on MNIST, reflecting harder density estimation in higher-dimensional spaces and underscoring the importance of a high-quality density estimator, whose accurate likelihoods minimize the scaler’s effect. Additional sensitivity analyses on the density scale parameter γ and on corrupted density estimates are provided in Appendix H, confirming robustness to density estimation imprecision.

Table 4: **Ablation study of DIP-EDL.** Individual and pairwise contributions of training set size, the density estimator, and the discriminative classifier on MNIST and CIFAR-10.

| Components | | | ID Performance | | OOD Performance Metrics | | | | | |
|------------|-----------------|-----------------|---------------------|---------------------|-------------------------|---------------|---------------------|---------------|-------------------------|---------------|
| | | | Acc. (\uparrow) | BS (\downarrow) | AUROC (\uparrow) | | AUPR (\uparrow) | | OOD BS (\downarrow) | |
| n | $DE_{X_i}^\psi$ | $NN_{X_i}^\phi$ | MNIST | | K-MNIST | Omniglot | K-MNIST | Omniglot | K-MNIST | Omniglot |
| ✓ | ✓ | × | 0.0980 | 0.9000 | 0.9998 | 0.9998 | 0.9996 | 0.9997 | 0.0000 | 0.0000 |
| ✓ | × | ✓ | 0.9958 | 0.0069 | 0.5138 | 0.5299 | 0.5742 | 0.6408 | 0.6826 | 0.7124 |
| × | ✓ | ✓ | 0.9952 | 0.7202 | 0.9996 | 0.9996 | 0.9992 | 0.9994 | 0.0000 | 0.0000 |
| ✓ | ✓ | ✓ | 0.9955 | 0.0079 | 0.9998 | 0.9998 | 0.9995 | 0.9997 | 0.0014 | 0.0000 |
| | | | CIFAR-10 | | CIFAR-100 | SVHN | CIFAR-100 | SVHN | CIFAR-100 | SVHN |
| ✓ | ✓ | × | 0.1000 | 0.9000 | 0.9000 | 0.9686 | 0.8864 | 0.9850 | 0.0000 | 0.0000 |
| ✓ | × | ✓ | 0.9496 | 0.0831 | 0.5036 | 0.5014 | 0.5014 | 0.7224 | 0.6945 | 0.6412 |
| × | ✓ | ✓ | 0.9496 | 0.7653 | 0.9000 | 0.9686 | 0.8864 | 0.9850 | 0.0004 | 0.0000 |
| ✓ | ✓ | ✓ | 0.9496 | 0.0978 | 0.9000 | 0.9686 | 0.8864 | 0.9850 | 0.3303 | 0.1032 |

4.6 ID Calibration

Standard neural networks often suffer from miscalibration, even with regularization [Guo et al., 2017, Vashistha and Farahi, 2025]. Conversely, DIP-EDL achieves calibration inherently through its probabilistic construction: as n grows, Dirichlet concentration parameters scale proportionally, yielding asymptotically calibrated ID predictions (see Theorem 3.2), as validated in Tables 1, 2, and 3.

5 Discussion

We provided a principled statistical interpretation of EDL as amortized VI in a hierarchical Bayesian model, clarifying the regularization parameter’s role and exposing its fundamental limitation. Particularly, EDL is unable to faithfully quantify uncertainty, leading to overconfidence on ID and OOD data. To address this, we introduced DIP-EDL, which decouples class prediction from uncertainty by scaling pseudo-counts with marginal covariate density, thus enabling distributional awareness. Theoretically, DIP-EDL achieves asymptotic concentration of the posterior to the true conditional distribution. Empirically, it outperforms established baselines (EDL, R-EDL, Re-EDL, DAEDL, PostNet, MC Dropout) in ID calibration and OOD detection on MNIST, CIFAR-10, and LAMOST.

The broader significance of this work lies in at least three directions. First, it provides a principled statistical foundation for EDL, clarifying its theoretical basis. Second, DIP-EDL generalizes the EDL framework by decoupling classification and uncertainty quantification, training each component independently; moreover, it applies to arbitrary classifier classes, including non-differentiable ones. Third, these gains come without sacrificing the practical efficiency of EDL: a single forward pass at inference time makes DIP-EDL a scalable and modular framework for reliable uncertainty-aware prediction. Future work could refine density estimation and establish finite-sample guarantees.

Acknowledgments

This work was supported by the NSF under Cooperative Agreement 2421782, the Simons Foundation grant MPS-AI-00010515 awarded to the NSF-Simons AI Institute for Cosmic Origins (CosmicAI), and the Giorgio Mortara scholarship by the Bank of Italy.

References

- Edmon Begoli, Tanmoy Bhattacharya, and Dimitri Kusnezov. The need for uncertainty quantification in machine-assisted medical decision making. *Nature Machine Intelligence*, 1(1):20–23, 2019.
- Viktor Bengs, Eyke Hüllermeier, and Willem Waegeman. Pitfalls of epistemic uncertainty quantification through loss minimisation. *Advances in Neural Information Processing Systems*, 35: 29205–29216, 2022.
- Viktor Bengs, Eyke Hüllermeier, and Willem Waegeman. On second-order scoring rules for epistemic uncertainty quantification. In *International Conference on Machine Learning*, pages 2078–2091. PMLR, 2023.
- Pier Giovanni Bissiri, Chris C Holmes, and Stephen G Walker. A general framework for updating belief distributions. *Journal of the Royal Statistical Society Series B: Statistical Methodology*, 78(5):1103–1130, 2016.
- Charles Blundell, Julien Cornebise, Koray Kavukcuoglu, and Daan Wierstra. Weight uncertainty in neural network. In *International conference on machine learning*, pages 1613–1622. PMLR, 2015.
- Ha Manh Bui and Anqi Liu. Density-regression: Efficient and distance-aware deep regressor for uncertainty estimation under distribution shifts. In *International Conference on Artificial Intelligence and Statistics*, pages 2998–3006. PMLR, 2024.
- Bertrand Charpentier, Daniel Zügner, and Stephan Günnemann. Posterior network: uncertainty estimation without ood samples via density-based pseudo-counts. In *Proceedings of the 34th International Conference on Neural Information Processing Systems, NIPS '20*, Red Hook, NY, USA, 2020. Curran Associates Inc. ISBN 9781713829546.
- Mengyuan Chen, Junyu Gao, and Changsheng Xu. R-EDL: Relaxing nonessential settings of evidential deep learning. In *The Twelfth International Conference on Learning Representations*, 2024a. URL <https://openreview.net/forum?id=Si3YFA641c>.
- Mengyuan Chen, Junyu Gao, and Changsheng Xu. R-edl: Relaxing nonessential settings of evidential deep learning. In *The Twelfth International Conference on Learning Representations*, 2024b.
- Mengyuan Chen, Junyu Gao, and Changsheng Xu. Revisiting essential and nonessential settings of evidential deep learning. *IEEE Transactions on Pattern Analysis and Machine Intelligence*, 2025.
- Tarin Clanuwat, Mikel Bober-Irizar, Asanobu Kitamoto, Alex Lamb, Kazuaki Yamamoto, and David Ha. Deep learning for classical japanese literature, 2018. URL <https://arxiv.org/abs/1812.01718>.
- Xiang-Qun Cui, Yong-Heng Zhao, Yao-Quan Chu, Guo-Ping Li, Qi Li, Li-Ping Zhang, Hong-Jun Su, Zheng-Qiu Yao, Ya-Nan Wang, Xiao-Zheng Xing, et al. The large sky area multi-object fiber spectroscopic telescope (lamost). *Research in Astronomy and Astrophysics*, 12(9):1197–1242, 2012.
- Danruo Deng, Guangyong Chen, Yang Yu, Furui Liu, and Pheng-Ann Heng. Uncertainty estimation by fisher information-based evidential deep learning. In *International conference on machine learning*, pages 7596–7616. PMLR, 2023.
- Li Deng. The mnist database of handwritten digit images for machine learning research [best of the web]. *IEEE Signal Processing Magazine*, 29(6):141–142, 2012. doi: 10.1109/MSP.2012.2211477.
- Conor Durkan, Artur Bekasov, Iain Murray, and George Papamakarios. nflows: normalizing flows in PyTorch, November 2020. URL <https://doi.org/10.5281/zenodo.4296287>.

- Yassir Fathullah and Mark JF Gales. Self-distribution distillation: efficient uncertainty estimation. In *Uncertainty in Artificial Intelligence*, pages 663–673. PMLR, 2022.
- Yarin Gal and Zoubin Ghahramani. Dropout as a bayesian approximation: Representing model uncertainty in deep learning. In *international conference on machine learning*, pages 1050–1059. PMLR, 2016.
- Yarin Gal, Petros Koumoutsakos, Francois Lanusse, Gilles Louppe, and Costas Papadimitriou. Bayesian uncertainty quantification for machine-learned models in physics. *Nature Reviews Physics*, 4(9):573–577, 2022.
- Junyu Gao, Mengyuan Chen, Liangyu Xiang, and Changsheng Xu. A comprehensive survey on evidential deep learning and its applications. *IEEE Transactions on Pattern Analysis and Machine Intelligence*, 2025.
- Isaac Gibbs, John J Cherian, and Emmanuel J Candès. Conformal prediction with conditional guarantees. *Journal of the Royal Statistical Society Series B: Statistical Methodology*, page qkaf008, 2025.
- Chuan Guo, Geoff Pleiss, Yu Sun, and Kilian Q Weinberger. On calibration of modern neural networks. In *International conference on machine learning*, pages 1321–1330. PMLR, 2017.
- Trevor J. Hastie and Robert Tibshirani. Discriminant analysis by gaussian mixtures. *Journal of the royal statistical society series b-methodological*, 58:155–176, 1996. URL <https://api.semanticscholar.org/CorpusID:118694839>.
- Manuel Haussmann, Sebastian Gerwinn, and Melih Kandemir. Bayesian evidential deep learning with pac regularization. *arXiv preprint arXiv:1906.00816*, 2019.
- Wenchong He, Zhe Jiang, Tingsong Xiao, Zelin Xu, and Yukun Li. A survey on uncertainty quantification methods for deep learning. *ACM Computing Surveys*, 2025.
- José Miguel Hernández-Lobato and Ryan Adams. Probabilistic backpropagation for scalable learning of bayesian neural networks. In *International conference on machine learning*, pages 1861–1869. PMLR, 2015.
- Geoffrey Hinton, Oriol Vinyals, and Jeff Dean. Distilling the knowledge in a neural network. *arXiv preprint arXiv:1503.02531*, 2015.
- Alex Krizhevsky. Learning multiple layers of features from tiny images. Technical report, University of Toronto, 2009.
- Alex Krizhevsky, Geoffrey Hinton, et al. Learning multiple layers of features from tiny images.(2009), 2009.
- Brenden M. Lake, Ruslan Salakhutdinov, and Joshua B. Tenenbaum. Human-level concept learning through probabilistic program induction. *Science*, 350(6266):1332–1338, 2015. doi: 10.1126/science.aab3050. URL <https://www.science.org/doi/abs/10.1126/science.aab3050>.
- Balaji Lakshminarayanan, Alexander Pritzel, and Charles Blundell. Simple and scalable predictive uncertainty estimation using deep ensembles. *Advances in neural information processing systems*, 30, 2017.
- Y. Lecun, L. Bottou, Y. Bengio, and P. Haffner. Gradient-based learning applied to document recognition. *Proceedings of the IEEE*, 86(11):2278–2324, 1998. doi: 10.1109/5.726791.
- Andrey Malinin and Mark Gales. Predictive uncertainty estimation via prior networks. *Advances in neural information processing systems*, 31, 2018.
- Andrey Malinin and Mark Gales. Reverse kl-divergence training of prior networks: Improved uncertainty and adversarial robustness. *Advances in neural information processing systems*, 32, 2019.
- Andrey Malinin, Bruno Mlodozeniec, and Mark Gales. Ensemble distribution distillation. *arXiv preprint arXiv:1905.00076*, 2019.

- Charles C Margossian and David M Blei. Amortized variational inference: When and why? *arXiv preprint arXiv:2307.11018*, 2023.
- Bálint Mucsányi, Michael Kirchhof, and Seong Joon Oh. Benchmarking uncertainty disentanglement: Specialized uncertainties for specialized tasks. *Advances in neural information processing systems*, 37:50972–51038, 2024.
- Jishnu Mukhoti, Andreas Kirsch, Joost van Amersfoort, Philip HS Torr, and Yarin Gal. Deep deterministic uncertainty: A simple baseline. *arXiv preprint arXiv:2102.11582*, 2021.
- Yuval Netzer, Tao Wang, Adam Coates, A. Bissacco, Bo Wu, and A. Ng. Reading digits in natural images with unsupervised feature learning. In *NIPS Workshop on Deep Learning and Unsupervised Feature Learning*, 2011. URL <https://api.semanticscholar.org/CorpusID:16852518>.
- George Papamakarios, Theo Pavlakou, and Iain Murray. Masked autoregressive flow for density estimation. In I. Guyon, U. Von Luxburg, S. Bengio, H. Wallach, R. Fergus, S. Vishwanathan, and R. Garnett, editors, *Advances in Neural Information Processing Systems*, volume 30. Curran Associates, Inc., 2017. URL https://proceedings.neurips.cc/paper_files/paper/2017/file/6c1da886822c67822bcf3679d04369fa-Paper.pdf.
- Adam Paszke, Sam Gross, Francisco Massa, Adam Lerer, James Bradbury, Gregory Chanan, Trevor Killeen, Zeming Lin, Natalia Gimelshein, Luca Antiga, Alban Desmaison, Andreas Köpf, Edward Yang, Zach DeVito, Martin Raison, Alykhan Tejani, Sasank Chilamkurthy, Benoit Steiner, Lu Fang, Junjie Bai, and Soumith Chintala. Pytorch: an imperative style, high-performance deep learning library. In *Proceedings of the 33rd International Conference on Neural Information Processing Systems*. Curran Associates Inc., Red Hook, NY, USA, 2019.
- Florian Seligmann, Philipp Becker, Michael Volpp, and Gerhard Neumann. Beyond deep ensembles: A large-scale evaluation of bayesian deep learning under distribution shift. *Advances in Neural Information Processing Systems*, 36:29372–29405, 2023.
- Murat Sensoy, Lance Kaplan, and Melih Kandemir. Evidential deep learning to quantify classification uncertainty. *Advances in neural information processing systems*, 31, 2018.
- Murat Sensoy, Lance Kaplan, Federico Cerutti, and Maryam Saleki. Uncertainty-aware deep classifiers using generative models. In *Proceedings of the AAAI Conference on Artificial Intelligence*, volume 34, pages 5620–5627, 2020.
- Maohao Shen, Jongha Jon Ryu, Soumya Ghosh, Yuheng Bu, Prasanna Sattigeri, Subhro Das, and Gregory Wornell. Are uncertainty quantification capabilities of evidential deep learning a mirage? *Advances in Neural Information Processing Systems*, 37:107830–107864, 2024.
- Ruijie Shi. LAMOST-Spectra-Classifer. <https://github.com/superdreamliner/LAMOST-Spectra-Classifer>. Accessed: [June 2, 2026].
- Theodoros Tsiligkaridis. Information robust dirichlet networks for predictive uncertainty estimation, April 8 2021. US Patent App. 17/064,046.
- Dennis Ulmer, Christian Hardmeier, and Jes Frellsen. Prior and posterior networks: A survey on evidential deep learning methods for uncertainty estimation. *arXiv preprint arXiv:2110.03051*, 2021.
- Peter Van Katwyk and Karianne J Bergen. Hybridflow: Quantification of aleatoric and epistemic uncertainty with a single hybrid model. *arXiv preprint arXiv:2510.05054*, 2025.
- Ritwik Vashistha and Arya Farahi. I-trustworthy models. a framework for trustworthiness evaluation of probabilistic classifiers. In *International Conference on Artificial Intelligence and Statistics*, pages 4726–4734. PMLR, 2025.
- Laura Ventura and Walter Racugno. Pseudo-likelihoods for bayesian inference. In *Topics on methodological and applied statistical inference*, pages 205–220. Springer, 2016.
- Hanjing Wang and Qiang Ji. Diversity-enhanced probabilistic ensemble for uncertainty estimation. In *Uncertainty in Artificial Intelligence*, pages 2214–2225. PMLR, 2023.

- Taeseong Yoon and Heeyoung Kim. Uncertainty estimation by density aware evidential deep learning. In *Proceedings of the 41st International Conference on Machine Learning, ICML'24*. JMLR.org, 2024.
- Sergey Zagoruyko and Nikos Komodakis. Wide residual networks. *arXiv preprint arXiv:1605.07146*, 2016.
- Xujiang Zhao, Yuzhe Ou, Lance Kaplan, Feng Chen, and Jin-Hee Cho. Quantifying classification uncertainty using regularized evidential neural networks. *arXiv preprint arXiv:1910.06864*, 2019.

A Reproducibility

The code to reproduce the results of the numerical experiments is available at: <https://github.com/NevenaGligic/DIP-EDL>.

B Related Literature.

This section contextualizes the proposed DIP-EDL method within the broader landscape of uncertainty quantification with EDL approaches. We first contrast our approach with existing EDL paradigms before summarizing the critical shortcomings identified in current EDL literature. For extensive surveys, we refer the reader to Ulmer et al. [2021] for EDL-specific developments and Shen et al. [2024] for a comprehensive overview of existing limitations.

B.1 Contrasting DIP-EDL with Existing EDL Paradigms

Following the taxonomy by Ulmer et al. [2021], EDL methods for Dirichlet-based classification are primarily distinguished by two criteria: (i) whether the network parameterizes the prior or the posterior Dirichlet distribution, and (ii) whether the training process incorporates OOD samples to enforce uncertainty calibration.

Regarding the first criterion, Ulmer et al. [2021] distinguish between *prior* and *posterior* networks. While both share a common optimization objective, balancing a predictive loss (e.g., cross-entropy) with an uncertainty-promoting regularizer (e.g., KL divergence toward a flat Dirichlet), their modeling mechanisms differ. Prior networks [Hausmann et al., 2019, Tsiligkaridis, 2021] parameterize an input-dependent concentration vector that defines a Dirichlet prior and derive the posterior via Bayes’ theorem given the observed labels. Conversely, posterior networks [Sensoy et al., 2018, Charpentier et al., 2020] bypass the explicit Bayesian update by directly predicting the pseudo-counts that define the concentration parameters of the Dirichlet posterior.

As for the second criterion, the idea is to train a model to output sharp Dirichlet distributions for in-distribution data and flat Dirichlet distributions for OOD data. Therefore, to achieve this kind of uncertainty calibration, the loss function is augmented with an additional regularization term, typically a KL divergence measure between the predicted Dirichlet distribution and a flat Dirichlet distribution, that penalizes confident predictions on OOD samples. In this paradigm, training is agnostic to the network type and can be applied to both prior [Malinin and Gales, 2018, 2019] and posterior [Zhao et al., 2019, Sensoy et al., 2020] network architectures.

While the aforementioned criteria categorize most EDL classification methods, certain approaches based on knowledge distillation [Hinton et al., 2015] fall outside this taxonomy. These methods transfer uncertainty estimates from a complex teacher model to a more efficient student EDL model, training the latter to mimic the teacher’s distributional output. Notable examples include Malinin et al. [2019], which distills the diversity of an ensemble into a single Dirichlet model, and Fathullah and Gales [2022], which leverages self-distillation from Gaussian stochastic dropout.

Another notable departure from the standard taxonomy is the Fisher Information-based EDL framework proposed by Deng et al. [2023]. This approach leverages the Fisher information of the Dirichlet distribution to quantify the informativeness of the evidence provided by each observation. By incorporating this metric, the model adjusts its concentration parameters, enhancing its sensitivity to evidence associated with uncertain or underrepresented classes.

B.2 Shortcomings of Existing EDL Approaches

Despite the growing popularity of EDL, several studies have identified fundamental limitations that challenge its ability to provide reliable uncertainty estimates. These critiques are summarized below.

More specifically, Bengs et al. [2022] demonstrated that loss minimization is not a theoretically viable framework for learning distributions over probability distributions, such as the Dirichlet distributions employed in EDL. A critical consequence of this result is that the distributional uncertainty in EDL models fails to vanish even in the asymptotic limit of infinite training data. Bengs et al. [2023] further extended this critique, proving that no loss function can successfully incentivize a second-order model to faithfully represent its epistemic uncertainty.

In a more recent theoretical analysis, Shen et al. [2024] generalized previous critiques by characterizing the optimal distribution targeted by standard EDL models. They demonstrated that this distribution depends fundamentally on a sample-size-independent regularization coefficient, leading to two critical conclusions: (i) EDL models fail to faithfully represent aleatoric uncertainty, as its quantification is governed by an arbitrary hyperparameter rather than solely by the DGP; and (ii) they cannot reliably capture epistemic uncertainty, because the predicted Dirichlet distributions fail to concentrate around the true conditional distribution—even in the asymptotic limit—due to this persistent dependence on the regularization term.

Other works, such as Chen et al. [2024b] have also correctly identified the issue of the fundamental dependence of EDL models on a regularization hyperparameter and proposed possible remedies to it. In particular, Chen et al. [2024b] introduced R-EDL, treats the regularization hyperparameter as an adjustable hyperparameter, as opposed to a fixed constant, and tunes it with respect to some performance metric (e.g., OOD detection AUROC) over a validation set. While this approach improves empirical performance, it does not address the fundamental theoretical limitations of EDL models identified in prior works.

C Proofs and Additional Derivations

We provide proofs for all propositions and theorems in the main text, beginning with a lemma on the Dirichlet distribution, which is stated without proof, as it is a well-known result.

Lemma C.1. Expectation of the Dirichlet Distribution. *If $p \sim \text{Dir}(\alpha)$ with $\alpha \in \mathbb{R}_+^K$, then*

$$\mathbb{E}[p(k)] = \frac{\alpha(k)}{\alpha_0}, \quad k = 1, \dots, K,$$

where $\alpha_0 = \sum_{k=1}^K \alpha(k)$.

C.1 Proof of Proposition 2.2

Proof. By Bayes' theorem, we have that

$$\begin{aligned} \pi_{Y_i}(p_i) &\propto f_{p_{1:n}}(Y_{1:n}) \pi(p_{1:n}) \\ &\propto f_{p_i}(Y_i) \pi(p_i) \\ &\propto \prod_{k=1}^K p_i(k)^{\mathbb{I}(Y_i=k)} \prod_{k=1}^K p_i(k)^{\alpha(k)-1} \\ &= \prod_{k=1}^K p_i(k)^{\alpha(k)+\mathbb{I}(Y_i=k)-1}. \end{aligned}$$

We recognize this as the kernel of a $\text{Dir}(\alpha + e_{Y_i})$, so

$$p_i \mid Y_{1:n} \sim \pi_{Y_i} = \text{Dir}(\alpha + e_{Y_i}).$$

Since the likelihood and prior factorize across observations, so does the joint posterior:

$$\pi_{Y_{1:n}}(p_{1:n}) \propto f_{p_{1:n}}(Y_{1:n}) \pi(p_{1:n}) = \prod_{i=1}^n f_{p_i}(Y_i) \pi(p_i) \propto \prod_{i=1}^n \pi_{Y_i}(p_i).$$

As a consequence, the posterior distribution of new class probabilities is equal to the prior:

$$\pi_{Y_{1:n}}(p_{n+1}) \propto \prod_{i=1}^n f_{p_i}(Y_i) \prod_{i=1}^{n+1} \pi(p_i) \propto \pi(p_{n+1}) = \text{Dir}(\alpha).$$

Finally, the posterior predictive distribution follows from Lemma C.1:

$$\begin{aligned}
\mathbb{P}(Y_{n+1} = k \mid Y_{1:n}) &= \int \mathbb{P}(Y_{n+1} = k \mid p_{n+1}) \pi_{Y_{1:n}}(p_{n+1}) dp_{n+1} \\
&= \int p_{n+1}(k) \pi(p_{n+1}) dp_{n+1} \\
&= \mathbb{E}_\pi[p_{n+1}(k)] \\
&= \frac{\alpha(k)}{\alpha_0}, \quad k = 1, \dots, K.
\end{aligned}$$

We conclude that

$$Y_{n+1} \mid Y_{1:n} \sim \text{Cat}\left(\frac{\alpha}{\alpha_0}\right).$$

□

C.2 Covariate-Indexed Categorical-Dirichlet Model

Definition C.2. Covariate-Indexed Categorical-Dirichlet Model. The model is defined as follows:

$$\begin{aligned}
Y_i \mid p_i &\stackrel{\text{i.i.d.}}{\sim} f_{p_i} = \text{Cat}(p_i), \quad i = 1, \dots, n, \\
p_i &= p_{X_i}, \quad X_i \stackrel{\text{i.i.d.}}{\sim} P_X^*, \\
p_j &\stackrel{\text{i.i.d.}}{\sim} \pi = \text{Dir}(\alpha), \quad j = 1, \dots, M_n,
\end{aligned}$$

for some $\alpha \in \mathbb{R}_+^K$, where $M_n = |\{X_{1:n}\}|$ is the number of distinct covariate values.

This model retains Dirichlet-Categorical conjugacy, enabling closed-form posterior inference.

Proposition C.3. *Given Definition C.2, the posterior and posterior predictive are*

$$\begin{aligned}
p_j \mid X_{1:n}, Y_{1:n} &\sim \text{Dir}(\alpha + c_j), \quad j = 1, \dots, M_n, \\
p_{1:M_n} \mid X_{1:n}, Y_{1:n} &\sim \prod_{j=1}^{M_n} \text{Dir}(\alpha + c_j), \\
Y_{n+1} \mid X_{1:n+1}, Y_{1:n} &\sim \text{Cat}\left(\frac{\alpha + c_x}{\alpha_0 + S_x}\right),
\end{aligned}$$

where $c_j = \sum_{i=1}^n \mathbb{I}(X_i = x_j^*) e_{Y_i}$ is the label count vector at x_j^* , $x_{1:M_n}^*$ are the distinct covariate values in $X_{1:n}$, $c_x = c_j$ if $x = x_j$ for some j and $\mathbf{0}_K$ otherwise, and $S_x = \sum_{k=1}^K c_x(k)$.

Proof. By Bayes' theorem, we have that

$$\begin{aligned}
\pi_{X_{1:n}, Y_{1:n}}(p_j) &\propto f_{p_{1:M_n}}(Y_{1:n} \mid X_{1:n}) \pi(p_{1:M_n} \mid X_{1:n}) \\
&= \prod_{i: X_i = x_j^*} f_{p_j}(Y_i) \pi(p_j) \\
&\propto \prod_{k=1}^K p_j(k)^{\sum_{i: X_i = x_j^*} \mathbb{I}(Y_i = k)} \prod_{k=1}^K p_j(k)^{\alpha(k) - 1} \\
&= \prod_{k=1}^K p_j(k)^{\alpha(k) + c_j(k) - 1}.
\end{aligned}$$

This is the kernel of a $\text{Dir}(\alpha + c_j)$, so

$$p_j \mid X_{1:n}, Y_{1:n} \sim \pi_{X_{1:n}, Y_{1:n}} = \text{Dir}(\alpha + c_j).$$

Since the likelihood and prior factorize across unique covariate values, so does the joint posterior:

$$\pi_{X_{1:n}, Y_{1:n}}(p_{1:M_n}) \propto f_{p_{1:M_n}}(Y_{1:n} \mid X_{1:n}) \pi(p_{1:M_n} \mid X_{1:n}) \propto \prod_{j=1}^{M_n} f_{p_j}(Y_{i: X_i = x_j^*}) \pi(p_j) \propto \prod_{j=1}^{M_n} \pi_{X_{1:n}, Y_{1:n}}(p_j).$$

As a consequence, the posterior distribution of new class probabilities is equal to the prior if the covariate is new and to the corresponding posterior if the covariate has been observed:

$$\begin{aligned} \pi_{X_{1:n+1}, Y_{1:n}}(p_{n+1}) &\propto f_{p_{1:M_n}}(Y_{1:n} | X_{1:n}) \pi(p_{1:M_n}, p_{n+1} | X_{1:n+1}) \\ &\propto \begin{cases} \pi(p_{n+1}) = \text{Dir}(\alpha), & \text{if } X_{n+1} \notin \{X_{1:n}\}, \\ \pi_{X_{1:n}, Y_{1:n}}(p_j) = \text{Dir}(\alpha + c_j), & \text{if } X_{n+1} = x_j^* \text{ for some } j = 1, \dots, M_n. \end{cases} \end{aligned}$$

Finally, the posterior predictive distribution follows from Lemma C.1:

$$\begin{aligned} \mathbb{P}(Y_{n+1} = k | X_{1:n+1}, Y_{1:n}) &= \int \mathbb{P}(Y_{n+1} = k | p_{n+1}) \pi_{X_{1:n+1}, Y_{1:n}}(p_{n+1}) dp_{n+1} \\ &= \int p_{n+1}(k) \pi_{X_{1:n+1}, Y_{1:n}}(p_{n+1}) dp_{n+1} \\ &= \mathbb{E}_{\pi_{X_{1:n+1}, Y_{1:n}}} [p_{n+1}(k)] \\ &= \begin{cases} \frac{\alpha(k)}{\alpha_0}, & \text{if } X_{n+1} \notin \{X_{1:n}\}, \\ \frac{\alpha(k) + c_j(k)}{\alpha_0 + \sum_{k=1}^K c_j(k)}, & \text{if } X_{n+1} = x_j^* \text{ for some } j = 1, \dots, M_n. \end{cases} \end{aligned}$$

□

C.3 Proof of Proposition 2.4

Proof. By Definition 2.3, the approximate posterior distribution of new class probabilities is

$$p_{n+1} | X_{n+1} \approx q_{X_{n+1}}^{\hat{\phi}_n} = \text{Dir} \left(\alpha + \text{NN}_{X_{n+1}}^{\hat{\phi}_n} \right).$$

Therefore, the posterior predictive distribution follows from Lemma C.1:

$$\begin{aligned} \mathbb{P}(Y_{n+1} = k | X_{1:n+1}, Y_{1:n}) &= \int \mathbb{P}(Y_{n+1} = k | p_{n+1}) q_{X_{n+1}}^{\hat{\phi}_n}(p_{n+1}) dp_{n+1} \\ &= \int p_{n+1}(k) q_{X_{n+1}}^{\hat{\phi}_n}(p_{n+1}) dp_{n+1} \\ &= \mathbb{E}_{q_{X_{n+1}}^{\hat{\phi}_n}} [p_{n+1}(k)] \\ &= \frac{\alpha(k) + \text{NN}_{X_{n+1}}^{\hat{\phi}_n}(k)}{\alpha_0 + \sum_{k=1}^K \text{NN}_{X_{n+1}}^{\hat{\phi}_n}(k)}. \end{aligned}$$

□

C.4 Proof of Proposition 2.5

Proof. Since both the variational distribution and the posterior factorize across observations, we have

$$\begin{aligned} \text{KL} \left(q_{X_{1:n}}^\phi \parallel \pi_{Y_{1:n}} \right) &= \mathbb{E}_{q_{X_{1:n}}^\phi} \left[\log \frac{\prod_{i=1}^n q_{X_i}^\phi(p_i)}{\prod_{i=1}^n \pi_{Y_i}(p_i)} \right] \\ &= \sum_{i=1}^n \mathbb{E}_{q_{X_i}^\phi} \left[\log \frac{q_{X_i}^\phi(p_i)}{\pi_{Y_i}(p_i)} \right] \\ &\propto \sum_{i=1}^n \mathbb{E}_{q_{X_i}^\phi} \left[\log \frac{q_{X_i}^\phi(p_i)}{f_{p_i}(Y_i) \pi(p_i)} \right] \\ &= \sum_{i=1}^n -\mathbb{E}_{q_{X_i}^\phi} [\log f_{p_i}(Y_i)] + \mathbb{E}_{q_{X_i}^\phi} \left[\log \frac{q_{X_i}^\phi(p_i)}{\pi(p_i)} \right] \\ &= \sum_{i=1}^n -\mathbb{E}_{q_{X_i}^\phi} [\log f_{p_i}(Y_i)] + \text{KL} \left(q_{X_i}^\phi \parallel \pi \right). \end{aligned}$$

□

C.5 Proof of Proposition 2.7

Proof. The proof follows the same steps as in the proof of Proposition 2.2, with the only difference being the tempered likelihood. Specifically, by Bayes' theorem, the posterior distribution of the class probabilities for each observation satisfies

$$\begin{aligned}\pi_{Y_i}^\nu(p_i) &\propto f_{p_{1:n}}(Y_{1:n})^\nu \pi(p_{1:n}) \\ &\propto f_{p_i}(Y_i)^\nu \pi(p_i) \\ &\propto \left(\prod_{k=1}^K p_i(k)^{\mathbb{I}(Y_i=k)} \right)^\nu \prod_{k=1}^K p_i(k)^{\alpha(k)-1} \\ &= \prod_{k=1}^K p_i(k)^{\alpha(k)+\nu \mathbb{I}(Y_i=k)-1}.\end{aligned}$$

This is the kernel of a $\text{Dir}(\alpha + \nu e_{Y_i})$, so

$$p_i \mid Y_{1:n} \sim \pi_{Y_i}^\nu = \text{Dir}(\alpha + \nu e_{Y_i}).$$

Since the likelihood and prior factorize across observations, so does the joint posterior:

$$\pi_{Y_{1:n}}^\nu(p_{1:n}) \propto f_{p_{1:n}}(Y_{1:n})^\nu \pi(p_{1:n}) \propto \prod_{i=1}^n f_{p_i}(Y_i)^\nu \pi(p_i) \propto \prod_{i=1}^n \pi_{Y_i}^\nu(p_i).$$

As a consequence, the posterior distribution of new class probabilities is equal to the prior:

$$\pi_{Y_{1:n}}^\nu(p_{n+1}) \propto \prod_{i=1}^n f_{p_i}(Y_i)^\nu \prod_{i=1}^{n+1} \pi(p_i) \propto \pi(p_{n+1}) = \text{Dir}(\alpha).$$

Finally, the posterior predictive distribution follows from Lemma C.1:

$$\begin{aligned}\mathbb{P}(Y_{n+1} = k \mid Y_{1:n}) &= \int \mathbb{P}(Y_{n+1} = k \mid p_{n+1}) \pi_{Y_{1:n}}^\nu(p_{n+1}) dp_{n+1} \\ &= \int p_{n+1}(k) \pi(p_{n+1}) dp_{n+1} \\ &= \mathbb{E}_\pi[p_{n+1}(k)] \\ &= \frac{\alpha(k)}{\alpha_0}.\end{aligned}$$

□

C.6 Proof of Theorem 2.9

Proof. By the same steps as in the proof of Proposition 2.5:

$$\begin{aligned}\text{KL}\left(q_{X_{1:n}}^\phi \parallel \pi_{Y_{1:n}}^\nu\right) &= \mathbb{E}_{q_{X_{1:n}}^\phi} \left[\log \frac{\prod_{i=1}^n q_{X_i}^\phi(p_i)}{\prod_{i=1}^n \pi_{Y_i}^\nu(p_i)} \right] \\ &= \sum_{i=1}^n \mathbb{E}_{q_{X_i}^\phi} \left[\log \frac{q_{X_i}^\phi(p_i)}{\pi_{Y_i}^\nu(p_i)} \right] \\ &\propto \sum_{i=1}^n \mathbb{E}_{q_{X_i}^\phi} \left[\log \frac{q_{X_i}^\phi(p_i)}{f_{p_i}(Y_i)^\nu \pi(p_i)} \right] \\ &= \sum_{i=1}^n -\nu \mathbb{E}_{q_{X_i}^\phi} [\log f_{p_i}(Y_i)] + \mathbb{E}_{q_{X_i}^\phi} \left[\log \frac{q_{X_i}^\phi(p_i)}{\pi(p_i)} \right] \\ &= \nu \sum_{i=1}^n -\mathbb{E}_{q_{X_i}^\phi} [\log f_{p_i}(Y_i)] + \frac{1}{\nu} \text{KL}\left(q_{X_i}^\phi \parallel \pi\right) \\ &= \nu \mathcal{L}^\nu(\phi; Y_{1:n}, X_{1:n}).\end{aligned}$$

Therefore, since ν is a positive constant, we have that

$$\hat{\phi}_n = \operatorname{argmin}_{\phi} \left\{ \text{KL} \left(q_{X_{1:n}}^{\phi} \parallel \pi_{Y_{1:n}}^{\nu} \right) \right\} = \operatorname{argmin}_{\phi} \left\{ \mathcal{L}^{\nu}(\phi; Y_{1:n}, X_{1:n}) \right\}.$$

□

C.7 Proof of Proposition 2.10

Let us begin with the following lemma on the properties of the KL divergence, which is stated without proof, as it is a standard result.

Lemma C.4. Properties of the Kullback-Leibler Divergence. *Let f and g be two probability density functions defined on the same probability space. Then, the KL divergence from f to g is non-negative:*

$$\text{KL}(f \parallel g) \geq 0,$$

with equality if and only if f and g are equal almost surely.

Proof. By Theorem 2.9, we have that

$$\min_{\phi \in \Phi} \left\{ \mathcal{L}^{\nu}(\phi; Y_{1:n}, X_{1:n}) \right\} = \frac{1}{\nu} \min_{\phi \in \Phi} \left\{ \text{KL} \left(q_{X_{1:n}}^{\phi} \parallel \pi_{Y_{1:n}}^{\nu} \right) \right\}.$$

If Φ is sufficiently expressive and the optimization procedure achieves the minimizer of the KL divergence, then by Lemma C.4, we have that

$$\text{KL} \left(q_{X_{1:n}}^{\hat{\phi}_n} \parallel \pi_{Y_{1:n}}^{\nu} \right) = 0,$$

which holds if and only if

$$q_{X_{1:n}}^{\hat{\phi}_n} = \pi_{Y_{1:n}}^{\nu}.$$

In turn, since both distributions factorize across observations, this is equivalent to requiring that

$$q_{X_i}^{\hat{\phi}_n} = \pi_{Y_i}^{\nu}, \quad \text{for } i = 1, \dots, n.$$

By Definitions 2.8 and 2.6, this is equivalent to

$$\text{Dir}(\alpha + \text{NN}_{X_i}^{\hat{\phi}_n}) = \text{Dir}(\alpha + \nu e_{Y_i}), \quad \text{for } i = 1, \dots, n,$$

which holds if and only if

$$\text{NN}_{X_i}^{\hat{\phi}_n} = \nu e_{Y_i}, \quad \text{for } i = 1, \dots, n.$$

□

C.8 Proof of Proposition 2.12

By Definition 2.11, the vacuity of the approximate posterior predictive distribution is as follows:

$$\begin{aligned} u \left(\alpha + \text{NN}_{X_{n+1}}^{\hat{\phi}_n} \right) &= \frac{K}{\alpha_0 + \sum_{k=1}^K \text{NN}_{X_{n+1}}^{\hat{\phi}_n}(k)} \\ &= \frac{K}{\alpha_0 + \sum_{k=1}^K \nu e_{Y_{n+1}}(k)} \\ &= \frac{K}{\alpha_0 + \nu}, \end{aligned}$$

where we used the perfect interpolation condition from Proposition 2.10 in the second step.

C.9 Proof of Theorem 2.14

We can rewrite the empirical risk as follows:

$$\begin{aligned} \hat{\mathcal{R}}_n^{\nu}(\phi) &= \frac{1}{n} \sum_{i=1}^n \text{KL} \left(q_{X_i}^{\phi} \parallel \pi_{Y_i}^{\nu} \right) \\ &= \frac{1}{n} \text{KL} \left(q_{X_{1:n}}^{\phi} \parallel \pi_{Y_{1:n}}^{\nu} \right) \\ &= \frac{\nu}{n} \mathcal{L}^{\frac{1}{\nu}}(\phi; Y_{1:n}, X_{1:n}), \end{aligned}$$

where in the last step we skipped the same steps as in the proof of Theorem 2.9.

C.10 Proof of Theorem 2.15

By the law of iterated expectations, we can rewrite the population risk as follows:

$$\begin{aligned}\mathcal{R}^\nu(\phi) &= \mathbb{E}_{P_X^*} \left[\mathbb{E}_{P_{Y|X}^*} \left[\text{KL} \left(q_X^\phi \parallel \pi_Y^\nu \right) \right] \right] \\ &= \mathbb{E}_{P_X^*} \left[\mathbb{E}_{P_{Y|X}^*} \left[\mathbb{E}_{q_X^\phi} \left[\log q_X^\phi(p) - \log \pi_Y^\nu(p) \right] \right] \right] \\ &= \mathbb{E}_{P_X^*} \left[\mathbb{E}_{q_X^\phi} \left[\log q_X^\phi(p) - \mathbb{E}_{P_{Y|X}^*} [\log \pi_Y^\nu(p)] \right] \right],\end{aligned}$$

where we interchanged the order of expectations in the last step, since the first term is independent of Y , and the second term involves an expectation over $P_{Y|X}^*$, which is a finite sum and can therefore be freely reordered with the expectation over the variational distribution.

Then, for each fixed X , by Gibb's variational principle, the population risk is minimized by choosing the parameter ϕ^* such that the variational distribution satisfies

$$\begin{aligned}q_X^{\phi^*} &\propto \exp \left(\mathbb{E}_{P_{Y|X}^*} [\log \pi_Y^\nu(p)] \right) \\ &= \exp \left(\mathbb{E}_{P_{Y|X}^*} [\log \text{Dir}(\alpha + \nu e_Y)] \right) \\ &= \exp \left(\mathbb{E}_{P_{Y|X}^*} \left[\sum_{k=1}^K (\alpha(k) + \nu e_Y(k) - 1) \log p(k) - \log B(\alpha + \nu e_Y) \right] \right) \\ &\propto \exp \left(\sum_{k=1}^K (\alpha(k) + \nu P_{Y|X}^*(k | X) - 1) \log p(k) \right) \\ &= \prod_{k=1}^K p(k)^{\alpha(k) + \nu P_{Y|X}^*(k|X) - 1},\end{aligned}$$

where B is the multivariate Beta function. We recognize this as the kernel of a $\text{Dir}(\alpha + \nu P_{Y|X}^*)$, so

$$q_X^{\phi^*} = \text{Dir} \left(\alpha + \nu P_{Y|X}^* \right).$$

C.11 Proof of Theorem 3.2

Under Definition 3.1, the approximate posterior mean is

$$\begin{aligned}\mathbb{E}[p_i | X_{1:n}, Y_{1:n}] &\approx \frac{\alpha + n \text{DE}_{X_i}^{\hat{\psi}_n} \text{NN}_{X_i}^{\hat{\psi}_n}}{\alpha_0 + n \text{DE}_{X_i}^{\hat{\psi}_n}} \\ &= \frac{\frac{\alpha}{n} + \text{DE}_{X_i}^{\hat{\psi}_n} \text{NN}_{X_i}^{\hat{\psi}_n}}{\frac{\alpha_0}{n} + \text{DE}_{X_i}^{\hat{\psi}_n}} \\ &\xrightarrow{p} \frac{P_X^*(X_i) P_{Y|X}^*(\cdot | X_i)}{P_X^*(X_i)} \\ &= P_{Y|X}^*(\cdot | X_i),\end{aligned}$$

where the convergence in probability follows from the consistency of the two neural networks, as stated in Theorem 3.2 and the continuous mapping theorem. Similarly, the approximate posterior

variance of the class probabilities is

$$\begin{aligned}
\text{Var}[p_i(k) \mid X_{1:n}, Y_{1:n}] &\approx \frac{\frac{\alpha+n \text{DE}_{X_i}^{\hat{\psi}_n} \text{NN}_{X_i}^{\hat{\psi}_n}(k)}{\alpha_0+n \text{DE}_{X_i}^{\hat{\psi}_n}} \left(1 - \frac{\alpha+n \text{DE}_{X_i}^{\hat{\psi}_n} \text{NN}_{X_i}^{\hat{\psi}_n}(k)}{\alpha_0+n \text{DE}_{X_i}^{\hat{\psi}_n}}\right)}{\alpha_0+n \text{DE}_{X_i}^{\hat{\psi}_n} + 1} \\
&= \frac{\frac{\frac{\alpha}{n} + \text{DE}_{X_i}^{\hat{\psi}_n} \text{NN}_{X_i}^{\hat{\psi}_n}(k)}{\frac{\alpha_0}{n} + \text{DE}_{X_i}^{\hat{\psi}_n}} \left(1 - \frac{\frac{\alpha}{n} + \text{DE}_{X_i}^{\hat{\psi}_n} \text{NN}_{X_i}^{\hat{\psi}_n}(k)}{\frac{\alpha_0}{n} + \text{DE}_{X_i}^{\hat{\psi}_n}}\right)}{\alpha_0+n \text{DE}_{X_i}^{\hat{\psi}_n} + 1} \\
&\approx \frac{\frac{P_X^*(X_i) P_{Y|X}^*(k|X_i)}{P_X^*(X_i)} \left(1 - \frac{P_X^*(X_i) P_{Y|X}^*(k|X_i)}{P_X^*(X_i)}\right)}{\alpha_0+n P_X^*(X_i) + 1} \\
&= \frac{P_{Y|X}^*(k \mid X_i) \left(1 - P_{Y|X}^*(k \mid X_i)\right)}{\alpha_0+n P_X^*(X_i) + 1} \\
&\xrightarrow{n} 0,
\end{aligned}$$

where the convergence in probability again follows from the consistency of the two neural networks and the continuous mapping theorem, while the final step follows from the fact that the denominator diverges to infinity as n goes to infinity.

Therefore, by Chebyshev’s inequality, we have that

$$\mathbb{P}(|p_i(k) - \mathbb{E}[p_i(k) \mid X_{1:n}, Y_{1:n}]| > \varepsilon \mid X_{1:n}, Y_{1:n}) \leq \frac{\text{Var}[p_i(k) \mid X_{1:n}, Y_{1:n}]}{\varepsilon^2} \xrightarrow{n} 0.$$

Hence, we have that

$$\begin{aligned}
\mathbb{P}(\|p_i - \mathbb{E}[p_i \mid X_{1:n}, Y_{1:n}]\|_1 > \varepsilon \mid X_{1:n}, Y_{1:n}) &= \mathbb{P}\left(\sum_{k=1}^K |p_i(k) - \mathbb{E}[p_i(k) \mid X_{1:n}, Y_{1:n}]| > \varepsilon \mid X_{1:n}, Y_{1:n}\right) \\
&\leq \sum_{k=1}^K \mathbb{P}\left(|p_i(k) - \mathbb{E}[p_i(k) \mid X_{1:n}, Y_{1:n}]| > \frac{\varepsilon}{K} \mid X_{1:n}, Y_{1:n}\right) \\
&\xrightarrow{n} 0.
\end{aligned}$$

Finally, by the triangular inequality we have that

$$\|p_i - P_{Y|X}^*(\cdot \mid X_i)\|_1 \leq \|p_i - \mathbb{E}[p_i \mid X_{1:n}, Y_{1:n}]\|_1 + \|\mathbb{E}[p_i \mid X_{1:n}, Y_{1:n}] - P_{Y|X}^*(\cdot \mid X_i)\|_1 \xrightarrow{n} 0$$

Therefore, $p_i \xrightarrow{L_1} P_{Y|X}^*(\cdot \mid X_i) \mid X_{1:n}, Y_{1:n}$, which implies that $p_i \xrightarrow{p} P_{Y|X}^*(\cdot \mid X_i) \mid X_{1:n}, Y_{1:n}$.

D Detailed Experimental Configuration

This appendix provides the precise model architectures, training hyperparameters, and data processing steps used in our experiments to ensure reproducibility. All experiments were implemented in PyTorch 2.6 Paszke et al. [2019] with CUDA 12.4. Experiments were run on NVIDIA RTX A4000 GPUs (16 GB) and on a high-performance computing cluster equipped with NVIDIA H100 GPUs.

D.1 MNIST Configuration for DIP-EDL

For the MNIST dataset Deng [2012], we employ an architecture operating in pixel space. The density estimator is implemented using the `nflows` library Durkan et al. [2020].

Backbone Architecture (LeNet-5). We utilize a standard LeNet-style Convolutional Neural Network Lecun et al. [1998].

Density Estimator (MAF). We employ a Masked Autoregressive Flow (MAF) Papamakarios et al. [2017] to model the data density directly on flattened 28×28 pixel inputs. The flow consists of 10

Table 5: LeNet-5 implementation details for MNIST.

| Layer Type | Specifications |
|---------------|---|
| Conv2d | In: 1, Out: 20, Kernel: 5×5 , Stride: 1, Pad: 2, ReLU |
| MaxPool2d | Kernel: 2×2 , Stride: 2 |
| Conv2d | In: 20, Out: 50, Kernel: 5×5 , Stride: 1, Pad: 0, ReLU |
| MaxPool2d | Kernel: 2×2 , Stride: 2 |
| Flatten | Output Dimension: 1250 ($50 \times 5 \times 5$) |
| Linear | In: 1250, Out: 500, ReLU |
| Dropout | $p = 0.5$ |
| Linear (Head) | In: 500, Out: 10 (No activation) |

autoregressive transforms, each implemented as a MADE network with 20 residual blocks and 1024 hidden units per block. We apply Batch Normalization between transforms to improve convergence.

Data Augmentation & Preprocessing. For the density estimator, we adhere to the preprocessing protocol established in Papamakarios et al. [2017].

1. **Dequantization:** We add uniform noise $u \sim U(0, 1)$ to the discrete pixel values $x \in \{0, \dots, 255\}$ to convert them into continuous variables: $x' = (x + u)/256$.
2. **Logit Transformation:** To map the bounded data $x' \in [0, 1]$ to the unconstrained real space \mathbb{R} required by the flow, we apply a logit transformation:

$$z = \text{logit}(\lambda + (1 - 2\lambda)x')$$

where $\lambda = 10^{-6}$ is a regularization parameter to prevent numerical instability at the boundaries.

No standard mean/variance normalization or geometric augmentations (e.g., rotation) were applied to the MNIST data.

Training Hyperparameters. The training hyperparameters used in this work are listed in Table 6.

Table 6: Training Hyperparameters for MNIST

| Parameter | Backbone (EDL) | Density Estimator (MAF) |
|-----------------|--------------------|------------------------------|
| Optimizer | Adam | Adam |
| Batch Size | 128 | 128 |
| Epochs | 50 | 50 |
| Learning Rate | 1×10^{-3} | 1×10^{-4} |
| Weight Decay | 5×10^{-3} | 1×10^{-5} |
| Scheduler | None | StepLR (Step: 5, Gamma: 0.5) |
| Annealing Steps | 10 Epochs | N/A |

D.2 CIFAR-10 Configuration for DIP-EDL

For CIFAR-10 dataset Krizhevsky et al. [2009], we utilize a WideResNet-28-10 backbone Zagoruyko and Komodakis [2016] and perform density estimation in the learned feature space.

Backbone Architecture. For a classifier, we use WideResNet-28-10 with pre-activation residual blocks (BatchNorm \rightarrow ReLU \rightarrow Conv) with widening factor 10, yielding 640-dimensional output embeddings. For training, we use SGD (lr = 0.1, momentum = 0.9, Nesterov, weight decay = 5×10^{-4} , cosine annealing over 100 epochs). Spectral Normalization is applied to all convolutional and linear layers, which regularizes the Lipschitz constant of the network and produces well-behaved feature representations suitable for post-hoc density estimation.

Density Estimator. GDA is fitted post-hoc on the frozen 640-dimensional embeddings using a clean, non-augmented pass over the training set, with full per-class covariance matrices. The resulting log-likelihoods are z-scored using training-set statistics before being used for further evaluation. GDA is fitted on the non-augmented view of the data, as augmented features degrade density estimates. The training set size is $N = 40,000$, reflecting the 80/20 train/validation split.

Data Augmentation & Preprocessing. We apply standard data augmentations during the classifier training. These include random cropping to 32×32 with padding of 4, random horizontal flipping with a probability of 0.5, and random rotation of ± 15 degrees. All images are normalized using the standard CIFAR-10 mean and standard deviation ($\mu = (0.4914, 0.4822, 0.4465)$, $\sigma = (0.2023, 0.1994, 0.2010)$).

Training Hyperparameters (CIFAR-10). The training hyperparameters used in this work are listed in Table 7.

Table 7: Training Hyperparameters for CIFAR-10

| Parameter | Value |
|---------------|---------------------------------------|
| Optimizer | SGD (momentum = 0.9, Nesterov) |
| Learning Rate | 0.1 |
| Weight Decay | 5×10^{-4} |
| Batch Size | 128 |
| Epochs | 100 |
| Dropout Rate | 0.3 |
| LR Scheduler | Cosine Annealing ($T_{\max} = 100$) |

D.3 LAMOST Configuration for DIP-EDL

Dataset. We use a subset of the LAMOST Data Release 9 (DR9) dataset, available at <https://www.lamost.org/dr9/>. The subset was created by <https://github.com/superdreamliner/LAMOST-Spectra-Classifer> (Shi) and it can be downloaded from https://www.dropbox.com/scl/fi/tp81mfopdqbe50vwhhhb/spectra_training_data.tar. The dataset is created by drawing a total of 100,000 good-quality spectra (signal-to-noise ratio > 10) from DR9, spanning three stellar object classes: galaxy, quasar, and star. All spectra are evenly interpolated over the wavelength range 3,900–9,000 Å with 3,000 data points per spectrum.

In our experiments, we use Galaxy and Quasar as the two in-distribution classes and hold out Star spectra as the OOD set. The data is partitioned into 60/20/20 train/validation/test splits prior to any feature extraction.

Data preprocessing. Following the Github repository which created this dataset (Shi), raw flux arrays undergo energy normalization followed by Savitzky–Golay smoothing (window length 10, polynomial order 3). A three-stage feature extraction is then applied:

1. **PCA:** 500 principal components fitted on the training spectra.
2. **Spectral line features:** Mean flux within a ± 3 Å window around six known emission/absorption lines ($H\alpha$ 6563, $H\beta$ 4861, $H\gamma$ 4340, $H\delta$ 4102, Mg b 5184, Na D 5890; wavelengths in Å), yielding 6 features.
3. **Statistical block features:** Each spectrum is divided into 50 equal-length blocks. Mean, variance, argmax, argmin, maximum, and minimum are computed per block, yielding 300 features.

The concatenated feature vector has dimension $500 + 6 + 300 = 806$, fed as a single-channel 1-D signal (1, 806) to the backbone.

Backbone Architecture (Multi-Branch 1D CNN). We use the architecture by Shi, a multi-branch 1D convolutional network designed for stellar spectra classification.

Density Estimator (GDA). GDA is fitted post-hoc on the frozen 32-dimensional penultimate features (output of Dense 3) using the training split, with full per-class covariance matrices. Log-likelihoods are z-scored (see Section D.4) using training-set statistics before use in evaluation.

Training Hyperparameters. The training hyperparameters used in this work are listed in Table 9.

D.4 Addressing underflow in DIP-EDL due to log-likelihoods with large negative magnitudes.

To ensure numerical stability, we address the scale of the output log-likelihoods. Raw log-densities in high-dimensional pixel space can take on large negative magnitudes (e.g., < -1000), leading to

Table 8: Multi-branch 1D CNN architecture for LAMOST.

| Component | Specifications |
|---------------------------------|--|
| Parallel branches | 5 branches, kernel sizes $k \in \{3, 5, 7, 9, 11\}$ |
| Per-branch block ($\times 3$) | Conv1d (32 filters, pad $\lfloor k/2 \rfloor$) \rightarrow BatchNorm1d \rightarrow ReLU \rightarrow MaxPool1d (3, stride 3) |
| Merge | Concatenate and flatten all branch outputs |
| Dense 1 | Linear \rightarrow BatchNorm1d \rightarrow ReLU, Out: 128 |
| Dense 2 | Linear \rightarrow BatchNorm1d \rightarrow ReLU, Out: 64 |
| Dense 3 | Linear \rightarrow BatchNorm1d \rightarrow ReLU, Out: 32 |
| Head | Linear, Out: 2 (no activation) |

Table 9: Training Hyperparameters for LAMOST

| Parameter | Value |
|---------------|--------------------|
| Optimizer | Adam |
| Learning Rate | 1×10^{-3} |
| Batch Size | 128 |
| Epochs | 50 |
| Weight Decay | None |
| LR Scheduler | None |

numerical underflow when exponentiated and converted to evidence. We mitigate this by Z-score normalizing the log-likelihoods using the mean and standard deviation statistics calculated on the In-Distribution (ID) training set.

D.5 Baseline Implementation Details

To ensure a rigorous and fair comparison, we utilize the official open-source implementations for all competing methods. For EDL Sensoy et al. [2018], MC Dropout Gal and Ghahramani [2016], and Deep Ensembles Lakshminarayanan et al. [2017], we align the backbone with DIP-EDL (LeNet-5 for MNIST, WideResNet-28-10 for CIFAR-10, and the multi-branch 1D CNN for LAMOST) to isolate the contribution of the uncertainty quantification mechanism. DAEDL Yoon and Kim [2024], R-EDL Chen et al. [2024a], Re-EDL Chen et al. [2025], and PostNet Charpentier et al. [2020] use their own backbone architectures as specified in their respective implementations for MNIST and CIFAR-10, while for LAMOST, where no official spectral architecture exists, DAEDL is adapted with a 1D convolutional backbone following its own architectural design, and R-EDL, Re-EDL, and PostNet are adapted to use linear backbones. The optimization hyperparameters for all baselines are detailed in Tables 10, 11, and 12.

Table 10: Baseline Training Hyperparameters (MNIST)

| Method | Epochs | Batch Size | LR | Optimizer | Specific Parameters |
|---------------|--------|------------|--------------------|-----------|--|
| EDL | 50 | 128 | 1×10^{-3} | Adam | Weight decay = 5×10^{-3} , KL annealing = 10 epochs |
| R-EDL | 60 | 64 | 1×10^{-3} | Adam | $\lambda_1 = 1.0, \lambda_2 = 0.1$ |
| Re-EDL | 60 | 64 | 1×10^{-3} | Adam | $\lambda_1 = 1.0, \lambda_2 = 0.1, \kappa = 0$ |
| DAEDL | 50 | 64 | 1×10^{-3} | Adam | Reg = 0.05, Dropout = 0.5 |
| PostNet | 50 | 64 | 5×10^{-5} | Adam | Latent dim = 6, Radial flow |
| MC Dropout | 50 | 128 | 1×10^{-3} | Adam | Dropout = 0.5, 50 MC samples |
| Deep Ensemble | 50 | 128 | 1×10^{-3} | Adam | 5 members |

E On the OOD Brier Score of DIP-EDL

We provide visual evidence for the claim in Section 4.3 that density estimation difficulty explains DIP-EDL’s higher OOD Brier Score on CIFAR-10. Figure 1 shows the predicted confidence distributions for ID and OOD samples on MNIST and CIFAR-10.

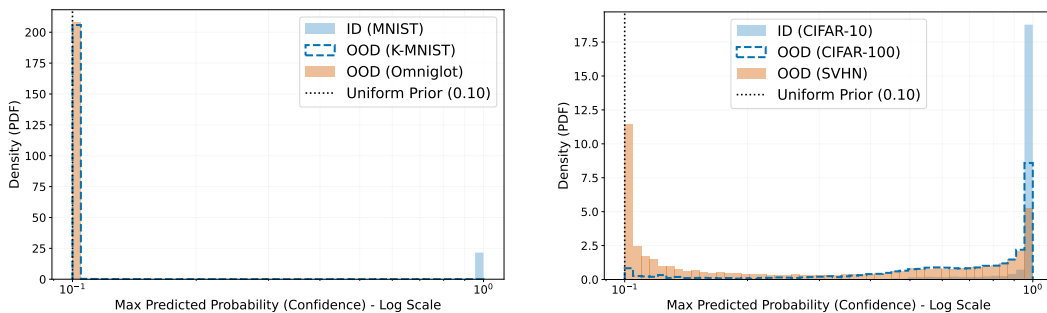
On MNIST, the density estimator assigns sufficiently low likelihoods to OOD inputs, driving their predicted confidence toward the uniform prior and yielding a near-zero OOD Brier Score. On CIFAR-10, density estimation in the higher-dimensional space is harder: likelihood estimates for OOD inputs remain large enough to sustain high classifier confidence, producing the larger OOD Brier Score discussed in Section 4.3, despite strong AUROC and AUPR performance.

Table 11: Baseline Training Hyperparameters (CIFAR-10)

| Method | Epochs | Batch Size | LR | Optimizer | Specific Parameters |
|---------------|--------|------------|--------------------|--------------|--|
| EDL | 100 | 128 | 0.1 | SGD (cosine) | Weight decay = 5×10^{-4} , KL annealing = 10 epochs |
| R-EDL | 200 | 64 | 1×10^{-4} | Adam | $\lambda_1 = 1.0, \lambda_2 = 0.1$ |
| Re-EDL | 200 | 64 | 1×10^{-4} | Adam | $\lambda_1 = 1.0, \lambda_2 = 0.8, \kappa = 0$ |
| DAEDL | 100 | 64 | 1×10^{-3} | Adam | Reg = 0.05, Dropout = 0.5 |
| PostNet | 200 | 64 | 5×10^{-4} | Adam | Latent dim = 6, Radial flow |
| MC Dropout | 100 | 128 | 0.1 | SGD (cosine) | Dropout = 0.3, 50 MC samples |
| Deep Ensemble | 100 | 128 | 0.1 | SGD (cosine) | 5 members |

Table 12: Baseline Training Hyperparameters (LAMOST)

| Method | Epochs | Batch Size | LR | Optimizer | Specific Parameters |
|---------------|--------|------------|--------------------|-----------|--|
| EDL | 50 | 128 | 1×10^{-3} | Adam | Weight decay = 1×10^{-4} , KL annealing = 10 epochs |
| R-EDL | 60 | 64 | 1×10^{-3} | Adam | $\lambda_1 = 1.0, \lambda_2 = 0.1$ |
| Re-EDL | 60 | 64 | 1×10^{-3} | Adam | $\lambda_1 = 1.0, \lambda_2 = 0.1, \kappa = 0$ |
| DAEDL | 50 | 64 | 1×10^{-3} | Adam | Reg = 0.05, Dropout = 0.5 |
| PostNet | 50 | 64 | 5×10^{-5} | Adam | Latent dim = 6, Radial flow |
| MC Dropout | 50 | 128 | 1×10^{-3} | Adam | Dropout = 0.5, 50 MC samples |
| Deep Ensemble | 50 | 128 | 1×10^{-3} | Adam | 5 members |



(a) MNIST (ID) vs. KMNIST and Omniglot (OOD) (b) CIFAR-10 (ID) vs. SVHN and CIFAR-100 (OOD)

Figure 1: **Predicted confidence distributions for DIP-EDL.** Confidence histograms for ID and OOD samples on MNIST (left) and CIFAR-10 (right).

F Ablation study - Full results

Tables 13a and 13b report the complete ablation results on MNIST and CIFAR-10, including all seven component configurations (individual, pairwise, and full model) discussed in Section 4.5.

G Toy Example: Vacuity Under Perfect Interpolation

To empirically validate Proposition 2.12 (that in-sample vacuity collapses to $\frac{K}{\alpha_0 + \nu}$ under perfect interpolation), we train a high-capacity neural network on a synthetic binary classification task designed to reach near-zero training error. We sample 100,000 observations from a balanced mixture of $\mathcal{N}([0, 0], I)$ and $\mathcal{N}([7, 7], I)$; the two components are well-separated, making near-perfect interpolation achievable by a sufficiently expressive model. We set the prior to $\alpha = [1, 1]^\top$ (so $\alpha_0 = 2$). The network uses 3 hidden layers with 64 ReLU units and a ReLU output layer to produce non-negative evidence values. It is trained with the EDL loss for 3000 iterations using Adam, and we repeat training across $\nu \in \{1, 5, 10, 50, 100, 500\}$ with a fixed random seed for reproducibility.

Table 14 shows that empirical vacuity tracks $\frac{K}{\alpha_0 + \nu}$ with high precision across all tested values of ν . As ν increases, the theoretical value $\frac{K}{\alpha_0 + \nu}$ decreases, reflecting a more informative prior; the empirical mean and median match this value closely in every case. The sharp concentration (near-zero standard deviation) confirms that, as the model approaches perfect interpolation, in-sample uncertainty is entirely determined by the arbitrary hyperparameter ν , irrespective of the data distribution. This confirms that standard EDL cannot distinguish epistemic from aleatoric uncertainty, and directly motivates the density-informed reparameterization in DIP-EDL.

Table 13: Full results of the ablation study of DIP-EDL.

(a) MNIST (ID) vs. K-MNIST and Omniglot (OOD)

| Components | | | ID Performance | | OOD Performance Metrics | | | | | |
|------------|-----------------|-----------------|---------------------|---------------------|-------------------------|---------------|---------------------|---------------|-------------------------|---------------|
| n | $DE_{X_i}^\psi$ | $NN_{X_i}^\phi$ | Acc. (\uparrow) | BS (\downarrow) | AUROC (\uparrow) | | AUPR (\uparrow) | | OOD BS (\downarrow) | |
| | | | | | K-MNIST | Omniglot | K-MNIST | Omniglot | K-MNIST | Omniglot |
| ✓ | ✓ | × | 0.0980 | 0.9000 | 0.9998 | 0.9998 | 0.9996 | 0.9997 | 0.0000 | 0.0000 |
| ✓ | × | ✓ | 0.9958 | 0.0069 | 0.5138 | 0.5299 | 0.5742 | 0.6408 | 0.6826 | 0.7124 |
| × | ✓ | ✓ | 0.9952 | 0.7202 | 0.9996 | 0.9996 | 0.9992 | 0.9994 | 0.0000 | 0.0000 |
| ✓ | ✓ | ✓ | 0.9955 | 0.0079 | 0.9998 | 0.9998 | 0.9995 | 0.9997 | 0.0014 | 0.0000 |
| ✓ | × | × | 0.0980 | 0.9000 | 0.5000 | 0.5000 | 0.5000 | 0.5686 | 0.0000 | 0.0000 |
| × | ✓ | × | 0.0980 | 0.9000 | 0.9997 | 0.9997 | 0.9993 | 0.9995 | 0.0000 | 0.0000 |
| × | × | ✓ | 0.9958 | 0.7446 | 0.5076 | 0.5174 | 0.5386 | 0.6021 | 0.0056 | 0.0059 |

(b) CIFAR-10 (ID) vs. CIFAR-100 and SVHN (OOD)

| Components | | | ID Performance | | OOD Performance Metrics | | | | | |
|------------|-----------------|-----------------|---------------------|---------------------|-------------------------|---------------|---------------------|---------------|-------------------------|---------------|
| n | $DE_{X_i}^\psi$ | $NN_{X_i}^\phi$ | Acc. (\uparrow) | BS (\downarrow) | AUROC (\uparrow) | | AUPR (\uparrow) | | OOD BS (\downarrow) | |
| | | | | | CIFAR-100 | SVHN | CIFAR-100 | SVHN | CIFAR-100 | SVHN |
| ✓ | ✓ | × | 0.1000 | 0.9000 | 0.9000 | 0.9686 | 0.8864 | 0.9850 | 0.0000 | 0.0000 |
| ✓ | × | ✓ | 0.9496 | 0.0831 | 0.5036 | 0.5014 | 0.5014 | 0.7224 | 0.6945 | 0.6412 |
| × | ✓ | ✓ | 0.9496 | 0.7653 | 0.9000 | 0.9686 | 0.8864 | 0.9850 | 0.0004 | 0.0000 |
| ✓ | ✓ | ✓ | 0.9496 | 0.0978 | 0.9000 | 0.9686 | 0.8864 | 0.9850 | 0.3303 | 0.1032 |
| ✓ | × | × | 0.1000 | 0.9000 | 0.5000 | 0.5000 | 0.5000 | 0.7225 | 0.0000 | 0.0000 |
| × | ✓ | × | 0.1000 | 0.9000 | 0.9000 | 0.9686 | 0.8864 | 0.9850 | 0.0000 | 0.0000 |
| × | × | ✓ | 0.9496 | 0.7536 | 0.5015 | 0.4991 | 0.5010 | 0.7222 | 0.0057 | 0.0053 |

Table 14: **Empirical vacuity under perfect interpolation.** In-sample vacuity statistics for different values of ν , compared to the theoretical prediction $\frac{K}{\alpha_0 + \nu}$ from Proposition 2.12.

| ν | $\frac{K}{\alpha_0 + \nu}$ | Mean | Std. Dev. |
|-------|----------------------------|-------|-----------|
| 1 | 0.667 | 0.667 | 0.0004 |
| 5 | 0.286 | 0.287 | 0.0021 |
| 10 | 0.167 | 0.167 | 0.0007 |
| 50 | 0.039 | 0.038 | 0.0002 |
| 100 | 0.020 | 0.020 | 0.0002 |
| 500 | 0.004 | 0.004 | 0.0005 |

H Density Robustness: Likelihood Scaling and Corruption

We run two experiments to assess the sensitivity of DIP-EDL with respect to the density estimator. In both cases, we verify that DIP-EDL remains robust to imprecision in the density estimate.

H.1 Likelihood Scaling (γ -sensitivity)

We introduce a scaling parameter $\gamma > 0$ so that concentration parameters become $\alpha = \mathbf{1} + \gamma \cdot n \cdot DE_X^\psi \cdot NN_X^\phi$, where $\gamma = 1$ corresponds to standard DIP-EDL. Tables 15 and 16 show results across two orders of magnitude of γ on MNIST and CIFAR-10. ID accuracy, AUROC, and AUPR remain essentially unchanged, demonstrating robustness to the overall scale of the density estimate. The only metric that varies with γ is OOD Brier Score, which increases monotonically as larger γ amplifies model confidence on OOD inputs, consistent with our discussion in Section 4.3.

Table 15: **Likelihood scaling (γ) on MNIST.** Effect of the likelihood scaling sensitivity parameter γ on ID accuracy, ID BS, AUROC, AUPR, and OOD BS, evaluated on MNIST.

| γ | ID Performance | | OOD Performance Metrics | | | | | |
|----------------------|---------------------|---------------------|-------------------------|---------|---------------------|---------|-------------------------|---------|
| | Acc. (\uparrow) | BS (\downarrow) | AUROC (\uparrow) | | AUPR (\uparrow) | | OOD BS (\downarrow) | |
| | | | MNIST | K-MNIST | Omniglot | K-MNIST | Omniglot | K-MNIST |
| 0.1 | 0.9951 | 0.0092 | 0.9997 | 0.9998 | 0.9995 | 0.9996 | 0.0005 | 0.0000 |
| 0.5 | 0.9951 | 0.0090 | 0.9997 | 0.9998 | 0.9995 | 0.9996 | 0.0012 | 0.0000 |
| 1.0 (DIP-EDL) | 0.9952 | 0.0088 | 0.9998 | 0.9999 | 0.9997 | 0.9998 | 0.0017 | 0.0000 |
| 2.0 | 0.9951 | 0.0089 | 0.9997 | 0.9998 | 0.9995 | 0.9996 | 0.0021 | 0.0000 |
| 5.0 | 0.9954 | 0.0087 | 0.9999 | 0.9999 | 0.9998 | 0.9999 | 0.0030 | 0.0000 |
| 10.0 | 0.9953 | 0.0088 | 0.9998 | 0.9999 | 0.9997 | 0.9998 | 0.0034 | 0.0000 |

Table 16: **Likelihood scaling (γ) on CIFAR-10.** Effect of the likelihood scaling sensitivity parameter γ on ID accuracy, ID BS, AUROC, AUPR, and OOD BS, evaluated on CIFAR-10.

| γ | ID Performance | | OOD Performance Metrics | | | | | |
|----------------------|---------------------|---------------------|-------------------------|-----------|---------------------|-----------|-------------------------|-----------|
| | Acc. (\uparrow) | BS (\downarrow) | AUROC (\uparrow) | | AUPR (\uparrow) | | OOD BS (\downarrow) | |
| | | | CIFAR-10 | CIFAR-100 | SVHN | CIFAR-100 | SVHN | CIFAR-100 |
| 0.1 | 0.9480 | 0.1148 | 0.9010 | 0.9630 | 0.8860 | 0.9819 | 0.2132 | 0.0604 |
| 0.5 | 0.9480 | 0.1029 | 0.9010 | 0.9630 | 0.8860 | 0.9819 | 0.2885 | 0.1009 |
| 1.0 (DIP-EDL) | 0.9480 | 0.0996 | 0.9010 | 0.9630 | 0.8860 | 0.9819 | 0.3206 | 0.1217 |
| 2.0 | 0.9480 | 0.0969 | 0.9010 | 0.9630 | 0.8860 | 0.9819 | 0.3518 | 0.1439 |
| 5.0 | 0.9480 | 0.0940 | 0.9010 | 0.9630 | 0.8860 | 0.9819 | 0.3911 | 0.1747 |
| 10.0 | 0.9480 | 0.0920 | 0.9010 | 0.9630 | 0.8860 | 0.9819 | 0.4191 | 0.1988 |

H.2 Density Corruption (σ -robustness)

We simulate degraded density estimates by injecting Gaussian noise $\mathcal{N}(0, \sigma^2)$ into the z-scored log-probability before computing DE_X^ψ . The case $\sigma = 0$ corresponds to the standard clean run, and $\sigma = \infty$ replaces the density entirely with i.i.d. $\mathcal{N}(0, 1)$ noise (a fully uninformative density estimator). Tables 17 and 18 show that DIP-EDL is very robust: all metrics remain essentially unchanged up to $\sigma = 2$, with graceful degradation at $\sigma = 5$. OOD detection becomes near-random only when the density estimator is fully uninformative ($\sigma = \infty$), consistent with the ablation results in Section 4.5.

Table 17: **Density corruption (σ) on MNIST.** Effect of Gaussian density corruption sensitivity parameter σ on ID accuracy, ID BS, AUROC, AUPR, and OOD BS, evaluated on MNIST.

| σ | ID Performance | | OOD Performance Metrics | | | | | |
|-----------|---------------------|---------------------|-------------------------|---------------------|---------------------|---------------------|-------------------------|---------------------|
| | Acc. (\uparrow) | BS (\downarrow) | AUROC (\uparrow) | | AUPR (\uparrow) | | OOD BS (\downarrow) | |
| | | | MNIST | K-MNIST | Omniglot | K-MNIST | Omniglot | K-MNIST |
| 0 (clean) | 0.9951 | 0.0089 | 0.9998 | 0.9998 | 0.9996 | 0.9997 | 0.0017 | 0.0000 |
| 0.5 | 0.9952 \pm 0.0001 | 0.0089 \pm 0.0001 | 0.9998 \pm 0.0001 | 0.9998 \pm 0.0001 | 0.9996 \pm 0.0001 | 0.9997 \pm 0.0001 | 0.0017 \pm 0.0000 | 0.0000 \pm 0.0000 |
| 1 | 0.9952 \pm 0.0001 | 0.0089 \pm 0.0001 | 0.9998 \pm 0.0001 | 0.9998 \pm 0.0001 | 0.9996 \pm 0.0001 | 0.9997 \pm 0.0001 | 0.0017 \pm 0.0001 | 0.0000 \pm 0.0000 |
| 2 | 0.9952 \pm 0.0001 | 0.0093 \pm 0.0002 | 0.9997 \pm 0.0001 | 0.9998 \pm 0.0001 | 0.9995 \pm 0.0001 | 0.9997 \pm 0.0001 | 0.0019 \pm 0.0001 | 0.0000 \pm 0.0000 |
| 5 | 0.9952 \pm 0.0001 | 0.0433 \pm 0.0008 | 0.9984 \pm 0.0001 | 0.9998 \pm 0.0001 | 0.9985 \pm 0.0001 | 0.9997 \pm 0.0001 | 0.0035 \pm 0.0002 | 0.0000 \pm 0.0000 |
| ∞ | 0.9955 \pm 0.0000 | 0.0078 \pm 0.0000 | 0.5016 \pm 0.0031 | 0.5023 \pm 0.0035 | 0.5010 \pm 0.0026 | 0.5707 \pm 0.0027 | 0.6957 \pm 0.0000 | 0.7443 \pm 0.0000 |

Table 18: **Density corruption (σ) on CIFAR-10.** Effect of Gaussian density corruption sensitivity parameter σ on ID accuracy, ID BS, AUROC, AUPR, and OOD BS, evaluated on CIFAR-10.

| σ | ID Performance | | OOD Performance Metrics | | | | | |
|----------|---------------------|---------------------|-------------------------|---------------------|---------------------|---------------------|-------------------------|---------------------|
| | Acc. (\uparrow) | BS (\downarrow) | AUROC (\uparrow) | | AUPR (\uparrow) | | OOD BS (\downarrow) | |
| | | | CIFAR-10 | CIFAR-100 | SVHN | CIFAR-100 | SVHN | CIFAR-100 |
| | 0 (clean) | 0.9480 | 0.0996 | 0.9010 | 0.9630 | 0.8860 | 0.9819 | 0.3206 |
| 0.5 | 0.9480 | 0.0996 \pm 0.0001 | 0.8988 \pm 0.0006 | 0.9623 \pm 0.0001 | 0.8848 \pm 0.0003 | 0.9817 \pm 0.0000 | 0.3202 \pm 0.0005 | 0.1220 \pm 0.0002 |
| 1 | 0.9480 | 0.1000 \pm 0.0002 | 0.8925 \pm 0.0010 | 0.9601 \pm 0.0003 | 0.8811 \pm 0.0006 | 0.9809 \pm 0.0001 | 0.3193 \pm 0.0009 | 0.1231 \pm 0.0002 |
| 2 | 0.9480 | 0.1023 \pm 0.0003 | 0.8734 \pm 0.0015 | 0.9514 \pm 0.0006 | 0.8682 \pm 0.0010 | 0.9778 \pm 0.0002 | 0.3167 \pm 0.0015 | 0.1274 \pm 0.0003 |
| 5 | 0.9480 | 0.1451 \pm 0.0011 | 0.8002 \pm 0.0027 | 0.8995 \pm 0.0017 | 0.8081 \pm 0.0021 | 0.9574 \pm 0.0006 | 0.3099 \pm 0.0010 | 0.1505 \pm 0.0008 |
| ∞ | 0.9480 | 0.0851 \pm 0.0000 | 0.5031 \pm 0.0040 | 0.5016 \pm 0.0056 | 0.5016 \pm 0.0046 | 0.7226 \pm 0.0039 | 0.7004 \pm 0.0000 | 0.6514 \pm 0.0000 |